

## FIELD TOPOLOGY ANALYSIS OF A LONG-LASTING CORONAL SIGMOID

A. S. SAVCHEVA<sup>1,2</sup>, A. A. VAN BALLEGOOIJEN<sup>2</sup>, AND E. E. DELUCA<sup>2</sup>

<sup>1</sup> Astronomy Department, Boston University, 725 Commonwealth Avenue, Boston, MA 02215, USA; [savcheva@bu.edu](mailto:savcheva@bu.edu)

<sup>2</sup> Harvard-Smithsonian Center for Astrophysics, 60 Garden Street, Cambridge, MA 02138, USA

Received 2011 September 8; accepted 2011 November 18; published 2011 December 14

### ABSTRACT

We present the first field topology analysis based on nonlinear force-free field (NLFFF) models of a long-lasting coronal sigmoid observed in 2007 February with the X-Ray Telescope on *Hinode*. The NLFFF models are built with the flux rope insertion method and give the three-dimensional coronal magnetic field as constrained by observed coronal loop structures and photospheric magnetograms. Based on these models, we have computed horizontal maps of the current and the squashing factor  $Q$  for 25 different heights in the corona for all six days of the evolution of the region. We use the squashing factor to quantify the degree of change of the field line linkage and to identify prominent quasi-separatrix layers (QSLs). We discuss the major properties of these QSL maps and devise a way to pick out important QSLs since our calculation cannot reach high values of  $Q$ . The complexity in the QSL maps reflects the high degree of fragmentation of the photospheric field. We find main QSLs and current concentrations that outline the flux rope cavity and that become characteristically S-shaped during the evolution of the sigmoid. We note that, although intermittent bald patches exist along the length of the sigmoid during its whole evolution, the flux rope remains stable for several days. However, shortly after the topology of the field exhibits hyperbolic flux tubes (HFT) on February 7 and February 12 the sigmoid loses equilibrium and produces two B-class flares and associated coronal mass ejections (CMEs). The location of the most elevated part of the HFT in our model coincides with the inferred locations of the two flares. Therefore, we suggest that the presence of an HFT in a coronal magnetic configuration may be an indication that the system is ready to erupt. We offer a scenario in which magnetic reconnection at the HFT drives the system toward the marginally stable state. Once this state is reached, loss of equilibrium occurs via the torus instability, producing a CME.

*Key words:* Sun: corona – Sun: flares – Sun: magnetic topology

*Online-only material:* color figures

### 1. INTRODUCTION

Solar eruptions, such as flares and coronal mass ejections (CMEs), are thought to originate from the conversion of free magnetic energy into kinetic and thermal energy of the released plasma in the process of reconnection. Free magnetic energy is most efficiently stored in sheared and twisted non-potential magnetic configurations (Priest & Forbes 2002). In such configurations, reconnection is thought to take place at the locations of strong and thin current sheets where breakdown of ideal magnetohydrodynamics (MHD) can occur and facilitate the reorganization of the magnetic field. Consequently, two of the main ingredients for producing solar eruptions are the storage of free magnetic energy and suitable conditions for reconnection. To further develop our understanding of these energetic processes we need to know the particular field and plasma dynamics and the conditions for any instabilities that might arise and lead to an eruption. Thus, understanding the detailed magnetic structure and topology of the magnetic field and current systems before, during, and after an eruption is essential for reconstructing and eventually forecasting solar eruptions.

In cases when an erupting active region (AR) is seen edge-on on the limb of the Sun, we can directly observe the geometry, configuration, and properties of coronal loops in and around it. The knowledge of which loops take part in the eruption, what their configurations are before and after the event, and the location of energy release gives us an idea of the magnetic field structure and how it evolves before and after the event. However, for eruptions close to the limb, magnetograms cannot give us detailed information about the surface magnetic

field. On the other hand, when flaring ARs are seen in projection on the solar disk, we lack the ability to observe the geometry and configuration of the coronal loops directly, but we do have reliable information about the photospheric magnetic flux distribution from line-of-sight (LoS) or vector magnetograms. In those cases, we can analyze the erupting regions by looking at MHD models and simulations or field extrapolations of the coronal magnetic field. So far, many such models have been employed for studying flaring ARs that are based on some information about the magnetic field in the regions. Generally, these methods belong to four distinct classes in increasing level of sophistication: potential field extrapolations (e.g., Démoulin et al. 1993); linear force-free extrapolation (e.g., Wang et al. 2000; Baker et al. 2009); nonlinear force-free field models from LoS magnetograms (NLFFF; e.g., Savcheva & van Ballegoijen 2009; Su et al. 2009, 2011) and NLFFF extrapolations from vector magnetograms (for a review see Schrijver et al. 2008); time-dependent MHD models based on a variety of driving mechanisms: footpoint motions (e.g., Aulanier et al. 2010), photospheric flux cancellation (e.g., Aulanier et al. 2010), or flux rope emergence (e.g., Fan & Gibson 2007; Archontis et al. 2009). Although dynamical MHD simulations are based on idealized magnetic field flux distributions and are not particularly constrained by observations, they can directly show how the magnetic configuration and the defining characteristics of an eruption develop in time. On the other hand, the data-driven and observationally constrained field extrapolations and magnetic models are static. For static models the time evolution can be followed by building separate independent models of a sequence of observations. Following the changes in the

three-dimensional (3D) magnetic field structure provides insight into the condition for eruption.

Early field topology analysis was conducted on idealized analytical configurations or basic potential (or linear force-free) extrapolations based on sample magnetic charge distributions (Démoulin et al. 1993, 1996a, 1997). This analysis was used to identify significant features that lead to eruptive behavior. The main topological features of the magnetic field that have been associated with preferred sites for formation of current sheets in ideal MHD are null points (NPs), separatrix surfaces, and separator field lines (Priest & Forbes 1989; Low & Wolfson 1988). These topological features separate the magnetic field volume in different connectivity domains. Field lines in those domains always connect to the same two magnetic sources and thus the field line linkage across separatrix surfaces is discontinuous. These features are the dominant sites for reconnection in 2D and 2.5D. However, they require special conditions of symmetry to remain present in 3D models (Hesse & Schindler 1988); even the slightest misalignment of the magnetic field vectors leads to the disappearance of these topological features. Indeed, after modeling the magnetic topology of several flaring ARs, Démoulin et al. (1997) showed that not all of the studied magnetic configurations contain NPs or separatrices that could explain the eruptions.

The generalization of separatrices in 3D are the so-called quasi-separatrix layers (QSLs; Priest & Forbes 1992; Priest & Démoulin 1995; Démoulin et al. 1996b). They are confined parts of the magnetic volume over which the field line linkage experiences dramatic changes but is nonetheless continuous, i.e., two field lines that start off close together in one flux element, diverge with distance but still connect to the same flux element at the other end. Like their 2D analogs, the locations and strength of QSLs carry information about the global topology of the magnetic field. However, they are much more ubiquitous than separatrix layers and are insensitive to small variations in the 3D magnetic field. This makes them more suitable tracers of the field linkage and topology that can be used always. Observationally, it has been shown (Démoulin et al. 1997) that even when NPs or separatrices are not present, one can always find strong QSLs close to the location of flare-associated  $H\alpha$  kernels or soft X-ray brightenings (Wang et al. 2000; Démoulin et al. 1997; Mandrini et al. 1997). Wang et al. (2000) and Baker et al. (2009) showed that AR outflows and heating are associated with main QSLs. These results demonstrate that QSLs are indeed ubiquitous topological features and finding the locations of prominent QSLs is as important for understanding the magnetic topology of flaring regions as are the NPs and separatrices.

Parker (1972) suggested that in the presence of smooth photospheric footpoint motions tangential discontinuities can form spontaneously in the coronal magnetic field (see also Parker 1983, 1987, 1994; Janse & Low 2009; Janse et al. 2010). Priest & Forbes (1989) considered steady magnetic reconnection in three dimensions and suggested that imposed boundary flows can produce reconnection at a so-called singular line with an X-type topology in a plane perpendicular to it. Démoulin et al. (1996b) discuss the same concept in the resistive case, where at a QSL field lines are forced to slip through the plasma at speeds of the order of the local Alfvén speed, thus causing the formation of a current sheet (see also slip-running reconnection; Aulanier et al. 2005). It has been debated whether random small-scale footpoint motions (magnetic flipping; Priest & Forbes 1992; Démoulin et al. 1996a) or special stagnation flows (Titov et al. 2003) are required for producing these current sheets.

When such current sheets become thin and concentrated enough, breakdown of ideal MHD can occur at small scales when the resistive or magnetic turbulence scales become important. Démoulin et al. (1996b) showed that the thickness of QSLs (related to the thickness of the associated current sheets) is inversely proportional to their strength (given by the norm of the Jacobian of the mapping of footpoints). In this sense, thin and strong QSLs can be used as markers of where fast reconnection can possibly occur. The energy stored in the surroundings of the current sheet at the location of the QSL can be released during reconnection. The MHD simulations of Aulanier et al. (2005) demonstrate that energy can accumulate around broader QSLs. The current distributions steepen with time (with continued boundary motions) and finally when a limiting thickness is reached explosive reconnection can release the energy. One might think that the exact limiting thickness may depend on the local plasma properties and the global field structure in the region, although such analysis has not yet been carried out.

MHD models (Aulanier et al. 2005, 2010), and potential and linear force-free field extrapolations (e.g., Démoulin et al. 1997; Wang et al. 2000) have been used to deduce the locations of prominent QSLs. These studies have been reasonably successful in modeling bipolar or quadrupolar configurations. However, when a region consists of sheared and twisted field lines overlaid by potential ones, it can be best understood by means of NLFFF models. Such regions, *sigmoids* (Rust & Kumar 1996), are known to have a characteristic S- or inverted-S shape and are most prominent in soft X-rays. Traditionally, sigmoids have been envisioned as having a twisted and sheared core field embedded in a potential envelope field (Moore & Roumeliotis 1992), which stabilizes the core field against eruption. Consequently, sigmoids have often been modeled as a twisted flux rope embedded in a potential arcade (Titov & Démoulin 1999). The process of flux rope creation differs from model to model. MHD simulations have employed flux rope emergence from below the photosphere (Fan & Gibson 2004, 2006, 2007; Archontis et al. 2009) or buildup of twist by flux cancellation (van Ballegoijen 1999; MacKay & van Ballegoijen 2006; Yeates et al. 2008) or shearing footpoint motions (Amari et al. 2000; Aulanier et al. 2005, 2010). For a thorough review of earlier sigmoid models one can refer to Green et al. (2007). Generally, the question of sigmoid formation and stability should be considered separately for emerging flux sites and long-lived sigmoids.

Observationally, it is evident that the hot S-shaped loops run on top of a curved polarity inversion line (PIL). Sigmoids have often been associated with  $H\alpha$  filaments (Rust & Kumar 1996; Gibson et al. 2002; Pevtsov 2002) that also lie along the PIL. The standard view is that the cool filamentary material accumulates in the dips of the twisted field lines of the core field. AR sigmoids are more transient (Sterling & Hudson 1997) than the quiescent ones (Leamon et al. 2003). According to Canfield et al. (1999, 2007), sigmoidal ARs are the preferred locations for CMEs and flares. This is not surprising since the sheared and twisted loops in these regions can store magnetic energy in stable structures and as the sigmoid evolves the energy grows (SvB09). If one wants to understand the structure and evolution of erupting regions, it is prudent to concentrate on sigmoidal regions since they have higher probability for producing eruptions. As a first step, it is most beneficial to concentrate on eruptions appearing in quiescent sigmoids, where the magnetic field configuration has not been utterly complicated by the presence and dynamics of sunspots, and the observed coronal loops are rather ordered.

In those cases gaining insight into the magnetic topology of such regions (via QSL analysis) and its evolution toward an eruption can prove to be a significant stepping stone for understanding CME- and flare-producing ARs. In addition, since sigmoids can be modeled as flux ropes, direct comparison can be made with the topology appearing in analytical flux rope configurations (Titov & Démoulin 1999; Démoulin et al. 1996b).

In this work, we analyze the magnetic topology and its evolution in the development of a long-lasting quiescent sigmoid in a decaying AR. The region is observed with the unprecedented spatial and temporal resolution of the X-Ray Telescope (XRT; Golub et al. 2007) on *Hinode* over its one week long evolution in 2007 February. The region was first described by McKenzie & Canfield (2008). In Savcheva & van Ballegoijen (2009, SvB09 hereafter), we presented a detailed description of the NLFFF models used to study the evolution of the magnetic field of the region over seven days leading to the B-class flare on 2007 February 12. Here we repeat this analysis and in addition include more careful modeling of the region preceding its first eruption on February 7, which was not considered in SvB09. The NLFFF models are based on the flux rope insertion method (van Ballegoijen 2004) and provides the 3D magnetic and current structure of the region. The topology analysis is conducted based on stable NLFFF models for all days of the evolution of the region. In a parallel study, we conduct higher resolution topology analysis of the model just before the flare on February 12 and make a detailed comparison with the MHD simulation of Aulanier et al. (2010).

In this paper, we present the first QSL analysis built upon a NLFFF model of a sigmoidal region. In Section 2, we briefly review the observations of the sigmoid. Section 3 is an overview of the flux rope insertion method and discusses refinements and new developments to the models presented in SvB09. In Section 4, we present the method used to calculate the locations and strength of QSLs. Section 5 gives an overview of the general properties of the QSL maps. Section 6 includes the main results about the QSL topology and evolution for the whole lifetime of the region. In Section 7, we concentrate on the models just before the two eruptions and show how QSLs can be utilized for pinpointing the location of both B-class flares and subsequent CMEs that the sigmoid produced. We present our discussion and conclusions in Section 8.

## 2. OBSERVATIONS

In the period 2007 February 6–12, *Hinode*/XRT performed high-resolution ( $1''$  pixel $^{-1}$ ) observations of a long-lasting coronal sigmoid (McKenzie & Canfield 2008). XRT provided high-cadence ( $\sim 30$  s) partial-disk ( $384'' \times 384''$ ) images in the thin-aluminum/polyimide filter between 06 UT on February 11 and 05:30 UT on February 12. The rest of the time the development of the sigmoid was tracked using full-disk synoptic images taken every 6 hr in the titanium/polyimide filter. These XRT observations give us a detailed view of the structure and dynamics of the hot X-ray loops outlining the sigmoid. The overall observed evolution of the region was described in detail in McKenzie & Canfield (2008) and SvB09. By following the regions' development in MDI magnetograms and XRT images we see that the sigmoidal shape builds up after two close-by bipolar regions merge. Initially, the northern part of the region is potential and the southern one is composed of sheared arcade loops. McKenzie & Canfield (2008) reported the occurrence of a B-class flare on February 12. Since XRT did not observe the region continuously in the early days of the evolution,

neither McKenzie & Canfield (2008) nor SvB09 reported the occurrence of another B-class flare followed by a CME and a coronal wave on February 7 at 20 UT, which were observed with EIT and *STEREO*. The overall loop structure of the region was preserved after the eruption and the development of its sigmoidal shape continued in the following days. The first S-shaped loops appeared on February 9 and the sigmoid was fully developed by February 11, showing S-shaped and two-J-like loops. The region produced a second B-class flare at 7:20 UT on February 12. After this, post-flare loops appeared in the middle of the region crossing the PIL at an almost right angle. In the following few hours the region was disrupted, although signs of an H $\alpha$  filament reappeared a day later and remained until February 14.

The radial photospheric magnetic flux distribution for the whole period is provided by MDI full-disk magnetograms with resolution  $4''$ . In addition, we obtain a synoptic Carrington magnetogram from SOLIS for Carrington rotation 2053. Both kinds of magnetograms are used to build the NLFFF models as described in the next section. Based on the total flux in the high-resolution MDI region, SvB09 determined that the region displays significant flux cancellation over its seven-day evolution.

In SvB09, we used *TRACE* 171 Å images taken on February 11 and 12 to show us the location of the dark filament seen in the extreme ultraviolet (EUV). Since *TRACE* and H $\alpha$  images were not available for the whole period, in this work we use *STEREO* 171 Å and 195 Å full-disk images to determine the location of the dark EUV filament for all days. The location, shape, and length of the observed filament are used to constrain the location and size of the flux rope, on which the NLFFF models are based.

## 3. THE NLFFF MODEL

Since sigmoids occupy regions of the corona where the plasma pressure is small compared to the magnetic pressure ( $\beta \ll 1$ ) and we assume that the corona is in equilibrium, the Lorentz force must be small ( $\mathbf{j} \times \mathbf{B} \approx 0$ ). The force-free condition is expressed by the assumption that any electric currents must flow parallel to the field lines:  $\nabla \times \mathbf{B}(\mathbf{r}) \approx \alpha(\mathbf{r})\mathbf{B}(\mathbf{r})$ , where  $\mathbf{B}(\mathbf{r})$  is the magnetic field as a function of position, and  $\alpha(\mathbf{r})$  is the so-called torsion parameter, which must be constant along field lines ( $\mathbf{B} \cdot \nabla \alpha = 0$ ). In a NLFFF,  $\alpha$  can be different along separate field lines while in linear force-free and potential models  $\alpha$  is constant (or zero) for the whole domain.

We model the core field of the sigmoid, composed of sheared and twisted magnetic field lines, as a weakly twisted flux rope, embedded in a potential arcade as has been traditionally done (Titov & Démoulin 1999). Unlike in the Titov & Démoulin flux rope model, the potential arcade is determined by the global photospheric magnetogram, rather than by idealized subphotospheric sources. The magnetic tension in the potential arcade counteracts the magnetic pressure in the flux rope and the whole configuration is held in equilibrium. The sigmoid is stable for over a week, so we require that our final models be in equilibrium as well.

A NLFFF model is constructed by inserting a weakly twisted coronal flux rope into a potential field model of the region, and relaxing the field to a force-free state using magneto-frictional relaxation (van Ballegoijen 2004). The flux-rope insertion method is described in detail in Bobra et al. (2008) and SvB09. Some improvements to the method have been

**Table 1**  
Summary of Best-fit Models

Date	$\Phi_{\text{axi}}$ ( $10^{20}$ Mx)	$F_{\text{pol}}$ ( $10^{10}$ Mx cm $^{-1}$ )	Pot. Energy ( $10^{31}$ erg)	Free Energy ( $10^{31}$ erg)	Relative Helicity ( $10^{41}$ Mx $^2$ )
Feb 6, 06:11 UT	3	0.5	7.87	$0.86 \pm 0.1$	$6.3 \pm 1.1$
Feb 7, 12:14 UT	7	1	6.22	$1.32 \pm 0.3$	$10.9 \pm 2.2$
Feb 8, 11:29 UT	3	1	4.31	$2.25 \pm 0.8$	$12.1 \pm 2.1$
Feb 9, 11:22 UT	5	1	4.79	$1.28 \pm 0.4$	$10.4 \pm 1.9$
Feb 10, 17:59 UT	5	1	4.15	$1.1 \pm 0.2$	$8.3 \pm 2.8$
Feb 11, 06:27 UT	5	1	4.01	$0.91 \pm 0.1$	$7.4 \pm 2.5$
Feb 12, 05:32 UT	3	1	3.52	$0.72 \pm 0.1$	$5.8 \pm 1.2$
Feb 12, 06:41 UT	5	5	3.64	$1.47 \pm 0.3$	$10.9 \pm 3.9$
Feb 12, 08:38 UT	5	1	3.49	$1.04 \pm 0.4$	$8.9 \pm 4.6$

recently incorporated. Hence, the models we present here are qualitatively similar to the ones discussed in SvB09, but these are more refined and robust by including the new boundary conditions and stability analysis, as discussed later. The model domain is wedge-shaped covering an area on the surface surrounding the sigmoid and extending from the solar surface to  $r \approx 2 R_{\odot}$ . The grid spacing is variable, as described in Bobra et al. (2008). The cell size on the photosphere in center of the modeled region is  $\delta\phi = 1.5 \times 10^{-3} R_{\odot}$ .

In its present form, the flux rope insertion method consists of the following steps. (1) The region of interest is centered on the sigmoid and is modeled at high spatial resolution ( $\sim 1$  Mm), using full-disk MDI magnetograms. We assume that  $B_r = B_{\parallel} / \cos \theta$ , where  $B_{\parallel}$  is the observed LoS magnetic field and  $\theta$  is the heliocentric angle. The regions farther away from the sigmoid are modeled with a lower resolution global potential field derived from a SOLIS synoptic map of  $B_r$ . This feature was not present in the modeling process in SvB09. The global field provides the side boundary conditions for the high-resolution region, while the upper boundary is left open (potential-field source surface model). (2) The magnetic flux distribution on the photosphere is modified by adding two oppositely directed circular flux sources at the two ends where the flux rope is to be anchored in the photosphere (both the global and the high-resolution fields are modified). Then the high-resolution and global potential fields are recomputed. Part of the domain is cleared by setting up a cavity with  $\mathbf{B} \approx \mathbf{0}$  where the flux rope is later inserted. The flux rope consists of an axial core field and poloidal field wrapped around it. Its initial parameters are height of the axis above the photosphere, width, axial flux ( $\Phi_{\text{axi}}$  in Mx) and poloidal flux per unit length ( $F_{\text{pol}}$  in Mx cm $^{-1}$ ). The flux rope path and length are chosen based on the location of the dark EUV filament seen in *STEREO*. (3) Initially this magnetic field configuration is not in equilibrium. We apply magneto-frictional relaxation which brings the field to equilibrium. The induction equation of the magneto-friction includes hyperdiffusion (Boozer 1986; Bhattacharjee & Hameiri 1986), which acts to suppress numerical artifacts while preserving the topology of the field. In this process the edges of the initial flux rope diffuse and it expands until the magnetic tension of the overlying potential arcade balances the magnetic pressure in the rope. The current distribution becomes diffused and smooth as well. (4) We perform stability and convergence diagnostics of the model. We seek that  $\alpha$  converges to nearly a constant along field lines with subsequent iterations as it is required by the NLFFF condition. Each model is additionally iterated without any diffusivity which allows the current distribution to concentrate and sharpen. The stability is checked again after this iteration and only then is the model flagged as stable if no further expansion

is observed. The latter was not performed in SvB09 but it was found to provide more stringent criteria for stability.

A grid of models (with different combinations of the poloidal and axial fluxes) are calculated for all days of the evolution of the sigmoid and special attention is given to the few hours before and after the flares. We select best-fit models from the set of stable models by matching model field lines to manually selected coronal loops from the corresponding XRT images. Figure 1 demonstrates four main steps of the modeling process. In Figure 1(a), we show some field lines traced from the global model, which provides a context for the sigmoid. In Figure 1(b), we show the path of the flux rope overlaid on a *STEREO* image of the dark EUV filament. Selected coronal loops, used for fitting the models are shown in Figure 1(c) and example field lines from the best-fit model are given in Figure 1(d). Field lines traced from the best-fit models for February 7, 9, 10, 11, and 12 are shown in Figure 2. They are compared to the corresponding XRT observations; one can clearly notice the sheared and twisted core of S- and J-shaped field lines, and the overlying potential arcade which prevails in the elbows of the sigmoid. In Table 1, we give a list of the best-fit flux rope parameters for all days.

#### 4. THE QSL CALCULATION

QSLs are places where the linkage of magnetic field lines changes drastically. Thus, the severity of this change is a measure of the strength of QSLs. The pioneering work of Priest & Démoulin (1995) showed that the gradient of the field line mapping from one set of footpoints to the other can be generally used to quantify the change in linkage. One footpoint with Cartesian coordinates  $(x_1, y_1)$  maps to the other footpoint with coordinates  $(x_2, y_2)$  in another part of the photosphere. The difference between the coordinates of the two footpoints is  $X = x_2 - x_1$  and  $Y = y_2 - y_1$ . In general,  $(X, Y)$  are some functions of  $(x, y)$  and this defines the mapping. The local gradient of the field line mapping is given by the Jacobian matrix (Priest & Démoulin 1995):

$$M = \begin{pmatrix} \frac{\partial X}{\partial x} & \frac{\partial X}{\partial y} \\ \frac{\partial Y}{\partial x} & \frac{\partial Y}{\partial y} \end{pmatrix} = \begin{pmatrix} a & b \\ c & d \end{pmatrix}. \quad (1)$$

Generally, one can pick a set of footpoints that lie on a circle. Then, the Jacobian matrix describes the mapping of this circle of footpoints (at the launching point) into an ellipse of footpoints at the target point. The ellipse can be rotated, squashed in a different degree, and/or have different area from the initial circle (Titov et al. 2002). When the circle is mapped into a

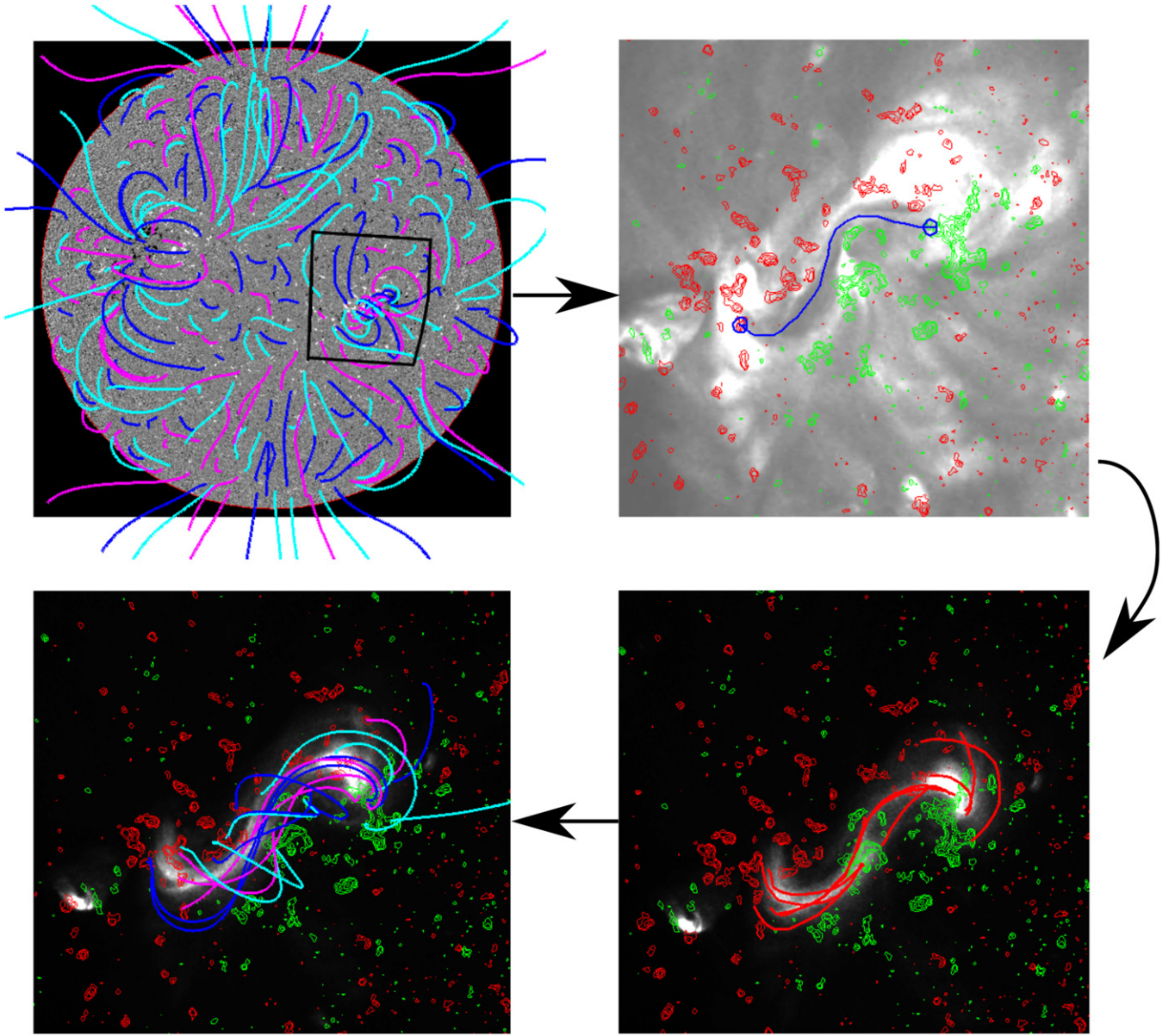


**Figure 1.** Diagram demonstrating the modeling process for achieving a NLFFF model. Some field lines traced from a global potential model overlaid on an MDI magnetogram (upper left). Flux rope path inserted on the location of dark EUV filament (blue line), the distribution of magnetic flux on the photosphere is shown with green (negative) and red (positive) contours (upper right). Coronal loops selected from an XRT image used to fit the models to the data (lower right). Sample field lines from the best-fit model (lower left).

(A color version of this figure is available in the online journal.)

line segment, we obtain a separatrix layer. The determinant of the Jacobian matrix (the Jacobian,  $\Delta$ ) describes the change of the area spanned by the footpoints. The norm,  $N$ , of the matrix gives the degree of stretching and compression (“squashing”) along the two perpendicular axes. Initially, a norm much larger than unity (large amount of stretching along one axis) was used to characterize a QSL, providing the degree of divergence of two field lines that start off within some small distance from each other (Priest & Démoulin 1995). However, the norm is not invariant with respect to the direction of the mapping, i.e., the norm of the Jacobian that maps  $(x_1, y_1)$  into  $(x_2, y_2)$  can be different from the norm of the inverse operation. In order to overcome this deficiency of  $N$ , Titov & Démoulin (1999) and Titov et al. (2002) proposed the use of the so-called squashing factor,  $Q$ , defined first only for rectangular coordinates and plane boundaries of the configuration volume. The covariant form of

$Q$ , applicable to any system of coordinates and shapes of the boundaries, was derived in Titov (2007). The squashing factor,  $Q$ , quantifies the strength of a QSL and is given by  $Q = N^2/|\Delta|$ , where  $N^2 \equiv a^2 + b^2 + c^2 + d^2$  and the Jacobian  $\Delta \equiv ad - bc$ . Assuming flux conservation, the Jacobian is also the ratio of the normal field components at the two footpoints,  $\Delta = B_z/B_z^*$ , where  $B_z$  is at  $(x_1, y_1)$  and  $B_z^*$  is at  $(x_2, y_2)$ .

It is evident from the above discussion that in order to calculate  $Q$  at a given point one needs to trace neighboring field lines from the 3D magnetic field. This is provided by the best-fit NLFFF model for each day, which we use to determine the properties of the mapping and study the time evolution of the field topology. We perform 2D QSL calculations for different horizontal slices at different heights in the corona. A separate finer grid than the original model grid is defined for the QSL calculation. At each fine grid point in the given horizontal slice

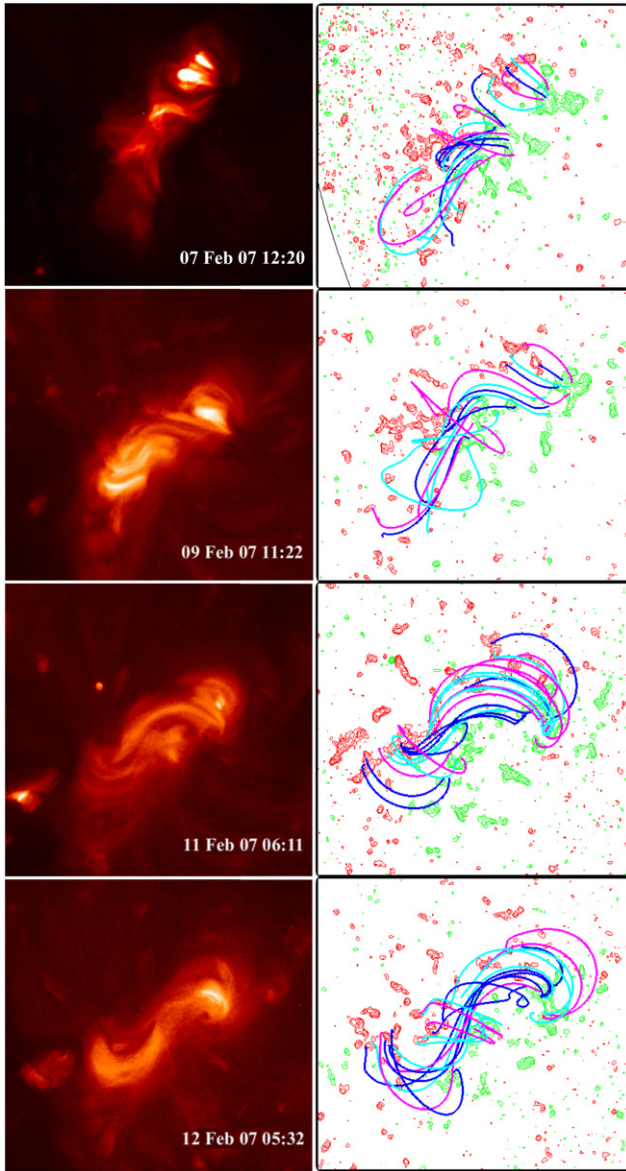


**Figure 2.** XRT images (left column) of different days of the evolution of the sigmoid. Sample field lines traced from the best-fit model for the corresponding XRT observation. The colors of the field lines are used to easily distinguish between the different field lines. The magnetic flux distribution is shown with green and red contours.

(A color version of this figure is available in the online journal.)

we trace a central field line and six neighboring field lines back to their footpoints on the photosphere. The method is schematically presented in Figure 3. Four points are in the same horizontal plane as the central one (green dot), one directly above and one below it (six red dots). In the figure, we show the central field line and one of the six neighboring field lines. All six points are projected in the shaded plane, perpendicular to the local magnetic field vector at the central point. We calculate the Jacobian matrix  $M_1$ , describing the gradient of the mapping of the six points in the plane  $(u, v)$  to one set of footpoints on the photosphere by performing a least-squares fit of the elements of the matrix. Similarly, we calculate  $M_2$  (Figure 3) to the other set of footpoints. The Jacobian matrix of the mapping from the first set of footpoints to the other is then given by  $M = M_2 M_1^{-1}$ . The least-squares fitting allows us to determine whether  $M_1$  and  $M_2$  are accurately measured, i.e., whether they accurately reproduce

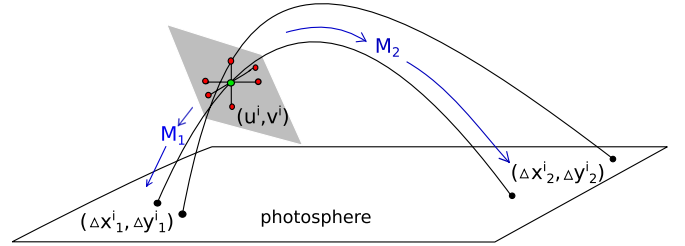


**Figure 3.** Schematic representation of the QSL calculation process. The central field is selected to pass through the green grid point in a given horizontal slice. Six neighboring field lines are traced from the six red dots down to the photosphere. The shaded plane is defined to be approximately perpendicular to the magnetic field vector at the green point. The gradient of the mapping of the field line footpoints in the shaded plane to the photosphere is determined.

(A color version of this figure is available in the online journal.)

the six footpoint positions. We require that these positions must be reproduced to within one cell size of the finer grid. When an accurate measurement of  $M_1$  and  $M_2$  cannot be made we set  $Q$  equal to a maximum value of 100. By using six starting points that do not all lie in a horizontal plane, we avoid the problems that would otherwise arise when the field lines are tangent to the plane. Finally,  $Q$  is calculated using the formalism of Titov et al. (2002). The norm is calculated from the Jacobian matrix  $M$ , but instead of dividing by the Jacobian to obtain  $Q$  we directly measure the vertical components of the magnetic field at the two ends of the central field line and take their ratio. This way we introduce less computational error when calculating  $Q$ . We compute the squashing factor in 25 different horizontal slices at different heights in our model from 2 ( $\approx 2100$  km) to 50 ( $\approx 52500$  km) cells above the photosphere, covering an area of  $200'' \times 140''$  around the sigmoid.

The grid size for the QSL calculation is 1/5 of the original model grid. The magnetic field between the original grid points is linearly interpolated to get down to the new grid size. This grid size is the minimum distance between two neighboring field lines at the launching point which in turn determines the maximum reliable value of  $Q$  which can be achieved. Minimum spacing of  $3 \times 10^{-4} R_\odot$  corresponds to a maximum reliable  $Q$  of a few hundred. The work of Démoulin et al. (1996a) and Démoulin et al. (1997) infers that when the norm reaches values of the order of at least  $10^3$  or more (or about  $10^6$  in  $Q$ ) the thickness of the QSLs (inversely proportional to  $M$ ) is small enough to allow reconnection to take place. Since the calculation of  $Q$  and the production of a QSL map is extremely computationally expensive, and our code is not particularly suited to this kind of calculation, we restrict ourselves to small values of  $Q$  ( $Q < 100$ ). Analysis of QSL maps with much higher  $Q$  values is planned for a future study. The disadvantage of looking at lower values of  $Q$  is that there are many QSLs with the same values that are picked out. Example of an original output QSL map is presented in Figure 4 and the general properties of the map are discussed in the next section.

Identifying the important QSLs requires further analysis. In order to determine which QSLs are important for the topology of the region, we conjecture that volumes that have both high values of  $Q$  and the current density,  $J$ , are the locations of significant QSLs. Parts of the domain that have relatively high  $Q$  in our calculations and low current density correspond to a volume where the field is nearly potential, away from the flux rope. On the other hand, the places where  $J$  is high correspond to highly non-potential fields associated with the flux rope. The

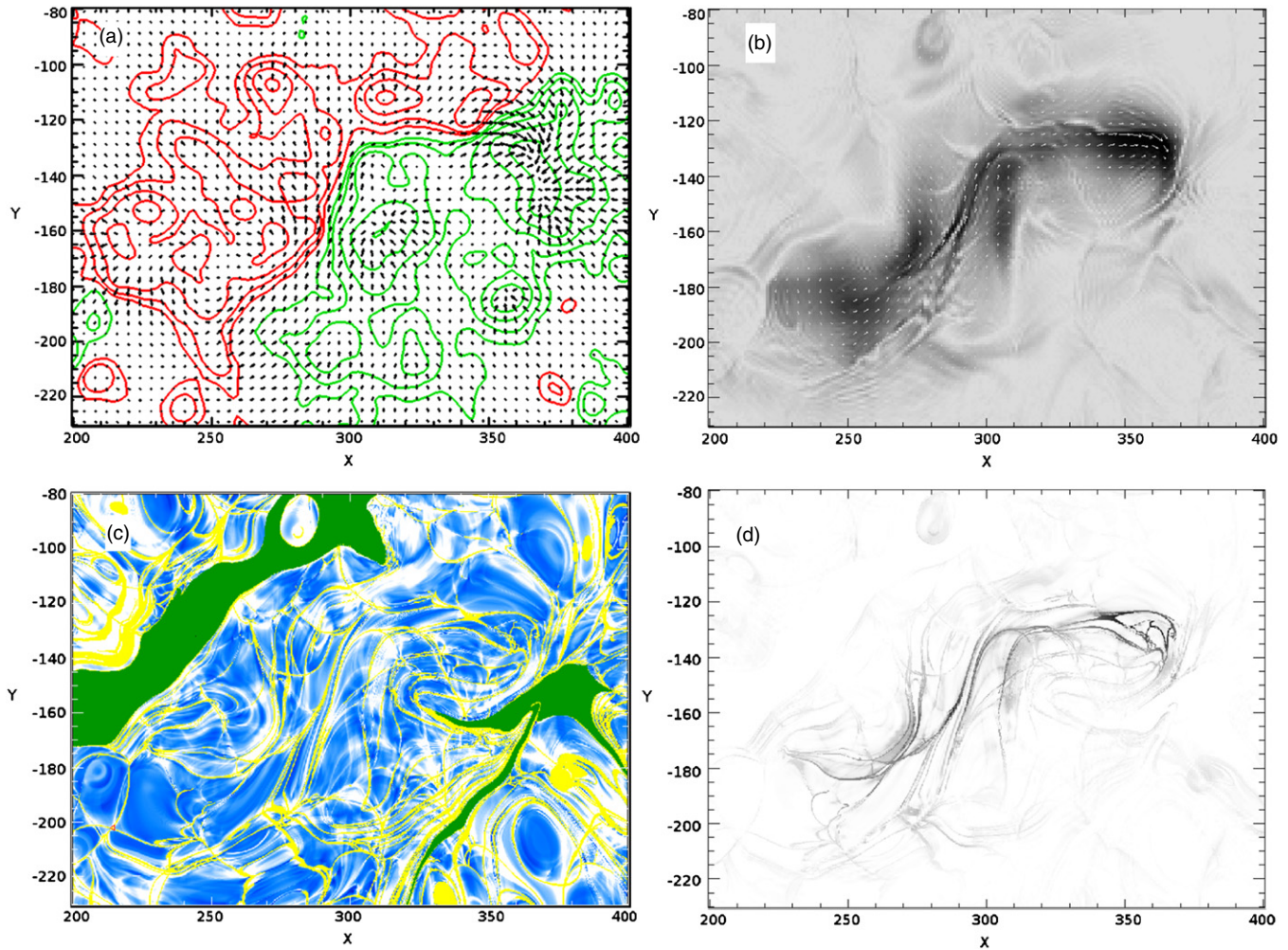


**Figure 4.** Magnetic field distribution in the computation domain for the QSL maps for February 12, 06:41 UT is shown in panel (a). The distribution is shown at height  $z = 6$  cells with green (negative) and red (positive) contours. The current density distribution in the same region at the same height is shown in panel (b); darker areas have higher current density. The corresponding QSL map is shown in panel (c). Blue areas have low  $Q$  values, lighter areas have higher  $Q$ , and yellow QSLs have the maximum  $Q$  that can be resolved by our calculation; green areas have field lines leaving the computation domain and  $Q$  cannot be determined for them. The  $JQ$  plot in panel (d) is a product of the distributions in panels (b) and (c). Darker areas are characterized by both high current density and high  $Q$ .

(A color version of this figure is available in the online journal.)

field in these volumes possesses high free energy which can be released in reconnection at the QSLs located in these areas, provided that  $Q$  gets high enough. The X-ray emission also seems to come from high- $J$  areas, as discussed later. On the other hand, if one looks at the whole QSL map with relatively high  $Q$  areas everywhere, one notices that away from the flux rope these high- $Q$  areas do not produce considerable emission in the X-rays, and hence they are not as relevant from observational stand point. Figure 4(d) shows a modified QSL map where the dark areas are high values of the product of  $Q$  and  $J$  (a  $JQ$  map). This method is far from exact since the relationships between the underlying diffuse current system and the presence of strong QSLs has not yet been determined theoretically or experimentally. Nonetheless, it can be seen from Figure 4 and the subsequent discussion that the  $JQ$  maps are successful at defining the QSLs that outline the flux rope, on which we concentrate our analysis.

## 5. GENERAL PROPERTIES OF QSL MAPS

In this section, we discuss several basic properties of the QSLs in relation to other quantities, such as the magnetic field and

current density. This is necessary for understanding how one can use the QSL analysis for gaining insight into how the topology of the sigmoid changes in time and what this implies about the structure and evolution of the AR. Our calculations are based on data-driven NLFFF models, which are characterized by large field complexity, an intrinsic property of observed magnetic fields. While some of the properties we discuss here are in general agreement with known analytical characteristics, most have not been discussed in the context of real magnetic fields and modeled current distributions.

In Figure 4, we show a contour map of the radial component of the magnetic field (panel (a)), map of the absolute value of the current density (panel (b)), an original QSL map (panel (c)), and a  $JQ$  plot (panel (d)) of the same region around the sigmoid. The vectors on the upper two panels show the direction of the magnetic field and current, respectively. All four maps are given for height of  $z = 6$  cells above the photosphere. High values of the current density are dark areas in the upper right plot. In the QSL map  $Q$  is plotted in different shades of blue, going from dark blue for the almost  $Q = 0$  areas to lighter blue and white for the higher values of  $Q$ . The yellow curves are QSLs where the value of  $Q$  is larger than what our calculation can

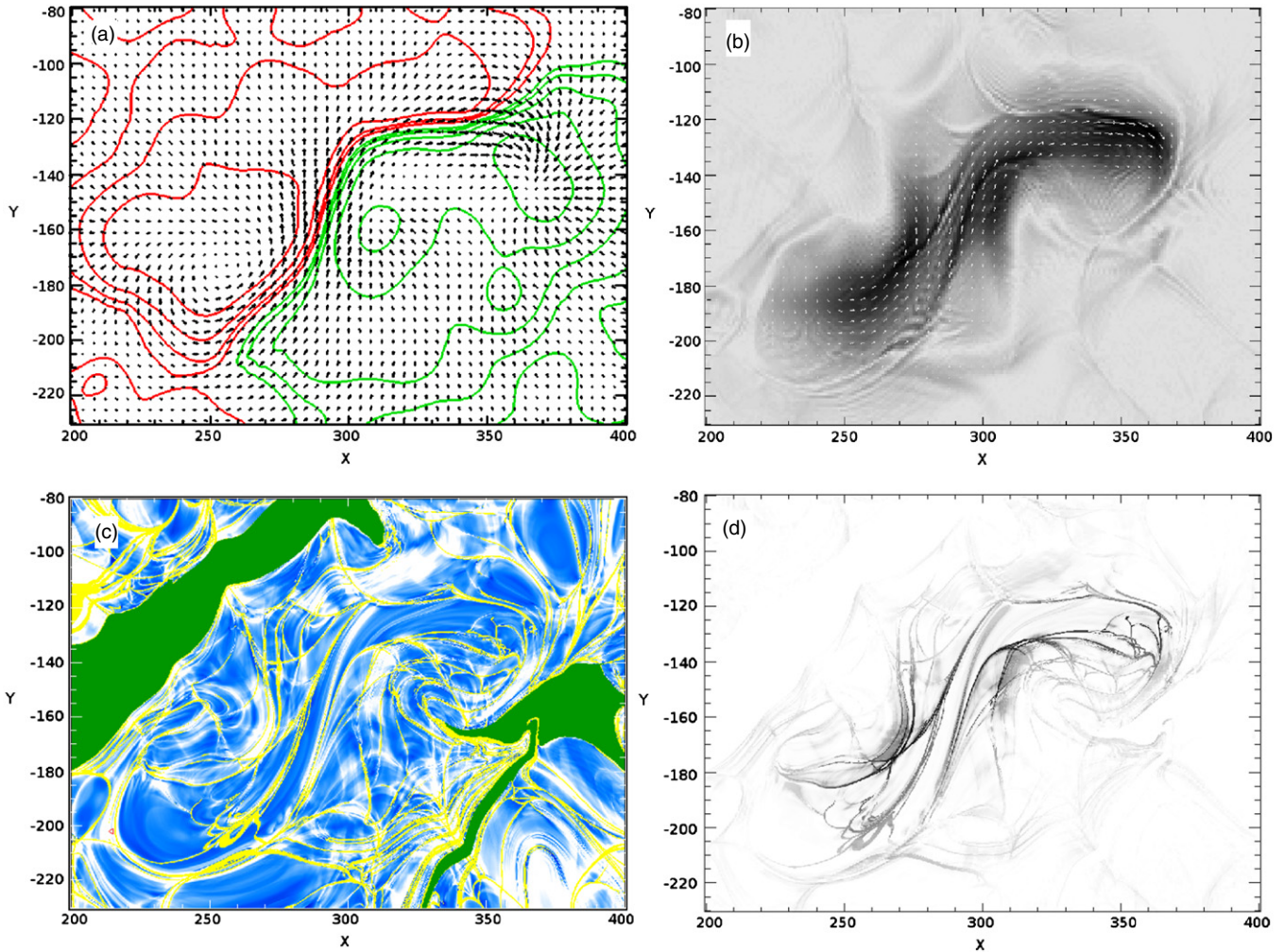


**Figure 5.** All panels are analogous to Figure 4 but for height  $z = 12$ .

(A color version of this figure is available in the online journal.)

resolve. Green areas are patches where the field lines leave the map domain at one end and hence  $Q$  cannot be calculated for them. The  $JQ$  plot in the lower right is obtained by multiplying the corresponding current density and QSL maps in the same figure, as discussed in the previous section.

The first striking property is that the magnetic field and the QSL distributions are both highly fragmented and complex. This is in contrast to the smooth magnetic field distributions and the small number of sharp strong QSLs obtained from theoretical considerations (Démoulin et al. 1996b; Titov 2007), MHD simulations (Aulanier et al. 2005, 2010), and potential and linear force-free extrapolations (Démoulin et al. 1993, 1997; Mandrini et al. 1997). As the fragmentation of the magnetic field decreases with height, the complexity of the QSLs also decreases. Figure 5 is analogous to Figure 4 but for a different height:  $z = 12$ . From comparing Figures 4 and 5 one can notice the transition to smoother magnetic field and  $Q$  distributions. In fact, going up in height the magnetic field vectors (and the main QSLs) become more and more misaligned with the PIL in the smooth transition between the flux rope core and the overlaying potential arcade and eventually turn perpendicular when the field is potential in the upper part of the computational domain. This transition of the shape, size, and orientation of the main QSLs can be best seen in the animated sequence of

consecutive QSL maps going up in height,<sup>3</sup> accompanied by similar animations of the magnetic field and current density.

By comparing the upper two panels of Figure 4 (and Figure 5) one can notice that the vectors of magnetic field and current are aligned, which is expected since the current is required to be parallel to the magnetic field for a NLFFF. The current density is higher close to the PIL since it is concentrated in the flux rope which lies along the PIL. Higher values of the current density are not necessarily associated with maxima in the magnetic field flux distribution. The main QSLs are also parallel to the magnetic field and current directions. This is much more apparent in the  $JQ$  plot. Also notice that the  $JQ$  product shows less variation in height. This further confirms the usefulness of this mask in highlighting important structures.

Magnetic field lines closely follow prominent QSLs along the length of the QSL and diverge at the footpoints by definition. It is still an open issue whether this bunching up of field lines at the main QSLs is associated with the accumulation of bright coronal loops in XRT images. Such an investigation is planned for a future work. A basic assumption of our model is that the soft X-ray emission outlines magnetic field lines. The soft X-ray emission in the sigmoid overlays characteristic S-like field lines traced from the prominent structures in the  $JQ$  maps.

<sup>3</sup> [http://hea-www.harvard.edu/~savcheva/sigmoid\\_qls.html](http://hea-www.harvard.edu/~savcheva/sigmoid_qls.html)

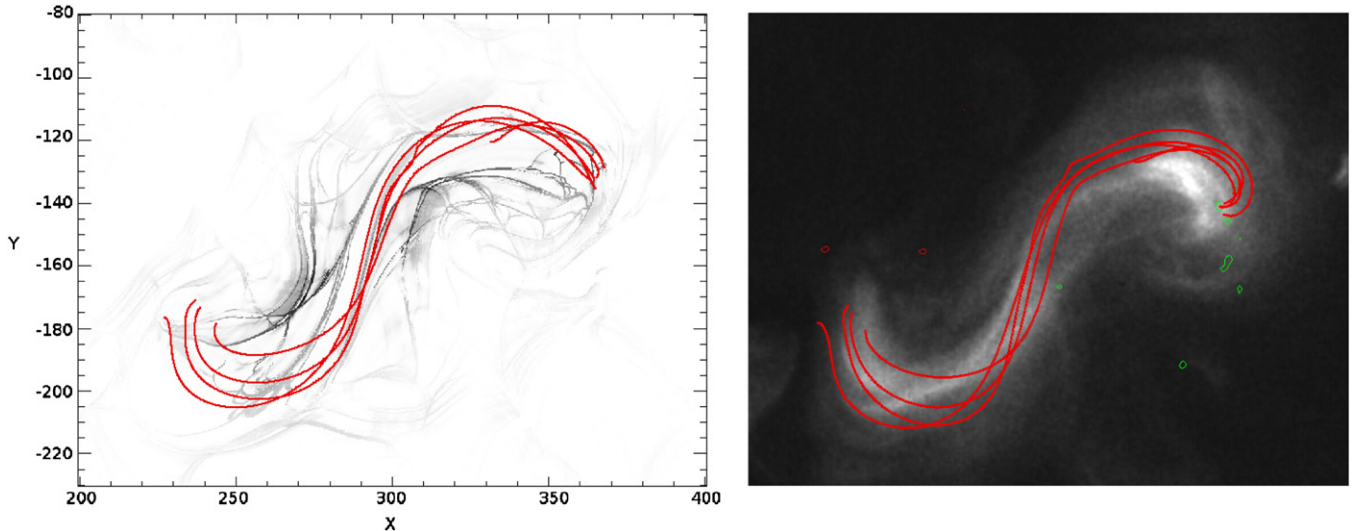


**Figure 6.**  $JQ$  analogous to Figure 5(d) is shown in the left panel. Some field lines are traced from the main QSLs on both sides of the PIL; they possess the characteristic S-shape. The same field lines are overlaid on the corresponding XRT image; one can notice that the field lines match the X-ray emission of the sigmoid.

(A color version of this figure is available in the online journal.)

In Figure 6 we show a set of field lines overlaid on the  $JQ$  map, and the same field lines overlaid on an XRT image of the sigmoid for 06:41 UT, February 12. The S-like field lines in the observation clearly coincide with X-ray shape of the region.

It has been proposed that main QSLs have to coincide with peaks in the current density as mentioned in Section 1. However, this is only proven to be true in the presence of footpoint motions. Our model is static and thus it is intrinsically impossible to recreate this effect. Instead, our current distributions are smooth as a result of the diffusion applied in the relaxation process. Nonetheless, the main QSLs coincide with somewhat sharp ridges in the current density and both outline the flux rope. In Figure 4 ( $z = 6$ ) the ridges in the current and the QSLs are closer together than in Figure 5 ( $z = 12$ ). For larger height they separate even more; later, they start to come back together and shorten. The main QSLs (and the ridges in the current) lie on the outside of the flux rope, which can be seen better in the flux rope cross sections shown in Figure 7. The upper two panels show a horizontal slice through the current at  $z = 12$  and a cross section through the flux rope at the location of the blue line. The lower panel shows the equivalent  $JQ$  horizontal slice and cross section. Currently we do not have the ability to perform high-resolution three-dimensional QSL calculations. Rather, the vertical cross section is composed of stacking 25 different horizontal maps and making a cut at the location of the blue line. Thus, the vertical resolution is poor but nonetheless the main characteristics are captured. The shapes of the QSLs in the horizontal maps for different heights and in vertical cross sections are schematically shown in Figure 8, where it can be seen how the QSLs outline the cavity of the flux rope.

The flux rope in our model has finite length and hence one can transition continuously from the envelope field to the core of the flux rope. As a consequence, it is topologically separated from the surrounding field by QSLs instead of true separatrices (as in the case of infinitely long flux ropes; see Schindler et al. 1988; Lau & Finn 1991). In addition, the region we are modeling is bipolar, so even though two neighboring field lines can have vastly different lengths and orientations (e.g., one belonging to the flux rope and one above it), they always start and end at

the same extended magnetic polarities. To visualize that high values of  $JQ$  (darker curves) are the locations where the field line connectivity drastically changes, Figure 9 shows a set of neighboring field lines traced from the model that are launched close together on different sides of three separate QSLs. Figure 9 demonstrates that field lines that start close together on both sides of a prominent QSL diverge with distance and connect to very different parts of the same major flux distribution. The short field line is part of the northern elbow of the sigmoid where the field is more potential, and the longer one runs close to the axis of the flux rope.

The shape of the main QSLs on the  $JQ$  plots is characteristic of a flux rope magnetic configuration. For comparison, we draw attention to the work of Démoulin et al. (1996b), Figure 1, and Titov (2007), Figure 4, where they discuss the shape of the QSLs associated with weakly twisted flux ropes. The characteristic QSL shapes at different heights are also shown on the schematic in Figure 8. Note that although our QSL maps show more complexity, the general shape of the main QSLs outlining the flux rope is similar to the analytical configurations discussed in those two papers. This is not surprising since the QSL shape reflects the global properties of the region and hence they should display similar characteristics for similar types of magnetic configurations. All QSL configurations discussed in the literature so far are given at the photosphere, where they show a characteristic hooked shape. In this sense, an important difference is that our QSLs at the bottom layer ( $z = 2$ ) form a continuous S-shaped cavity instead of the two horseshoe-like hooks at the locations where the flux rope is rooted in the photosphere in the analytical models. As discussed in Titov (2007), the value of  $Q$  along the main QSLs separating the flux rope from the surroundings varies substantially, from  $10^2$  to  $10^6$  in his model, and hence when displaying only the highest values of  $Q$  one would obtain just the hook-like shape of those QSLs. Since we do not have a way of distinguishing between the values of  $Q$  in the range  $10^3$ – $10^6$  our  $JQ$  plots effectively display the whole QSL regardless of the exact value. A higher resolution QSL calculation, included in a parallel study, will be able to distinguish between different high values of  $Q$  and show a more similar shape to those in Titov (2007).

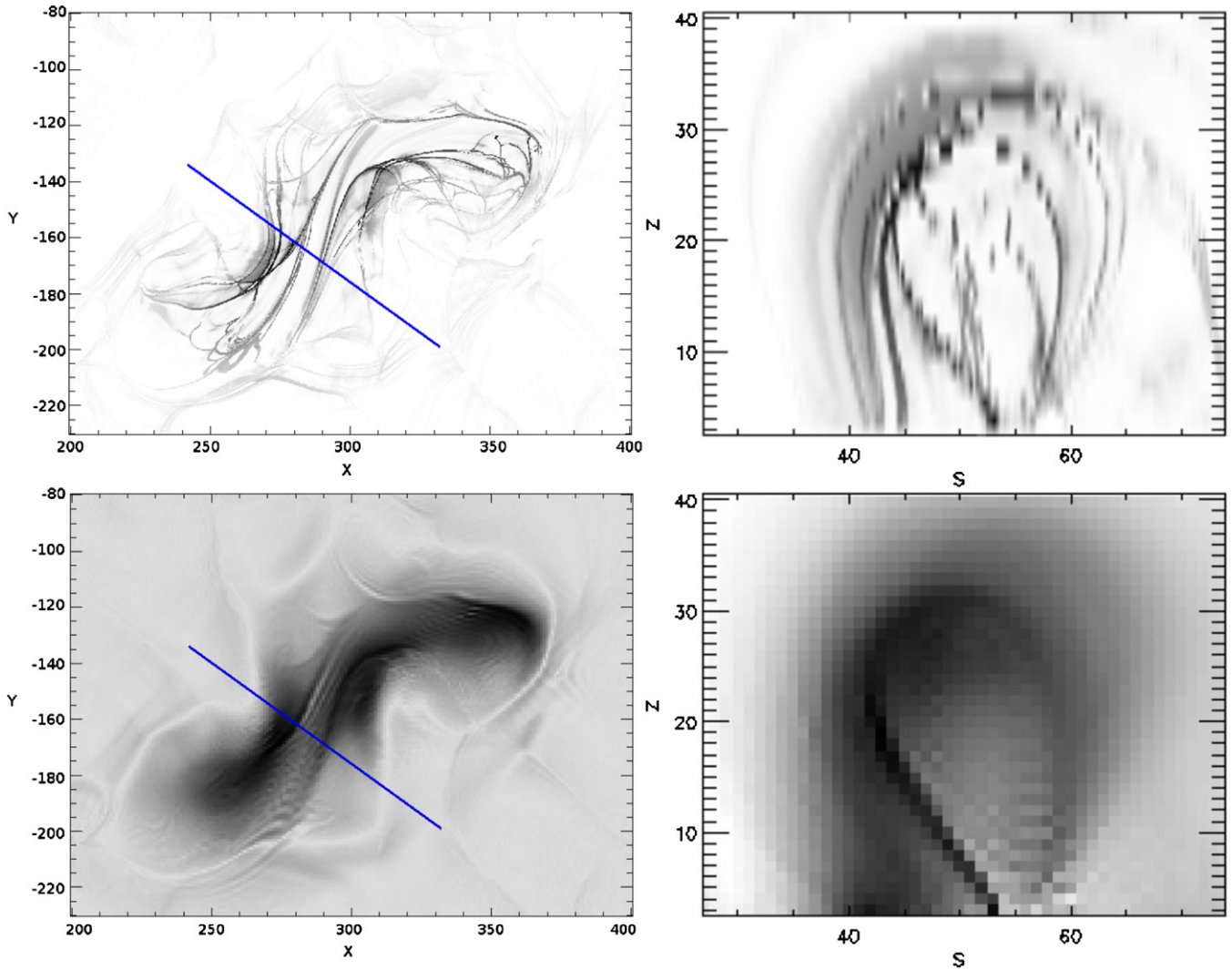


**Figure 7.** Current density and  $JQ$  plots analogous to Figures 5 (b) and (d). Cross sections through the flux rope at the location of the blue line are shown in the left column. The cuts are at the same location, demonstrating the similarity between the current and  $Q$  distributions in the flux rope.

(A color version of this figure is available in the online journal.)

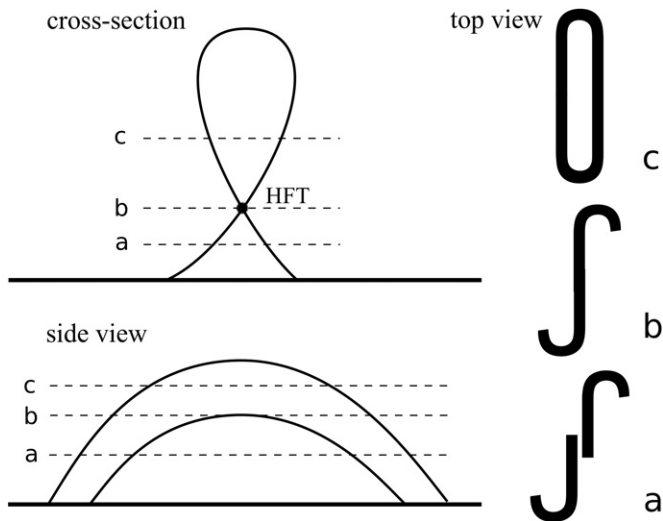


**Figure 8.** Schematic representation of the QSL topology in cross section (upper left), side view of the flux rope (lower left), and top views (right) at the locations of the horizontal lines: (a) under the HFT, (b) at the HFT, and (c) above the HFT.

## 6. THE PRE-ERUPTION EVOLUTION OF THE REGION

As mentioned in Section 2, this sigmoid has been observed to consistently evolve toward a coherent S-shape over a period of one week. After the joining of the two bipolar regions into a more extended region, the southern part of the region shows signs of large shear and some twist early on, while the northern part remains more potential until the full sigmoidal shape develops. This evolution of the type of field lines that compose the sigmoid over its evolution can be seen from Figure 2, where we have shown model field lines for several days. Figure 10 shows representative current density (left column) and  $JQ$  (right column) maps for the different days of the evolution of the region. The maps for February 7 and 12 are discussed in the next section. We have already discussed that the shape of main field lines follows closely the shape of the prominent QSLs. By following the evolution in the corresponding panels of Figures 2 and 10 one can see that the main QSLs in the earlier days have a slight S-shape which becomes more and more pronounced as we approach the eruption on February 12.

The first set of maps are for February 8, one day following the eruption on February 7. The sigmoid has started to develop

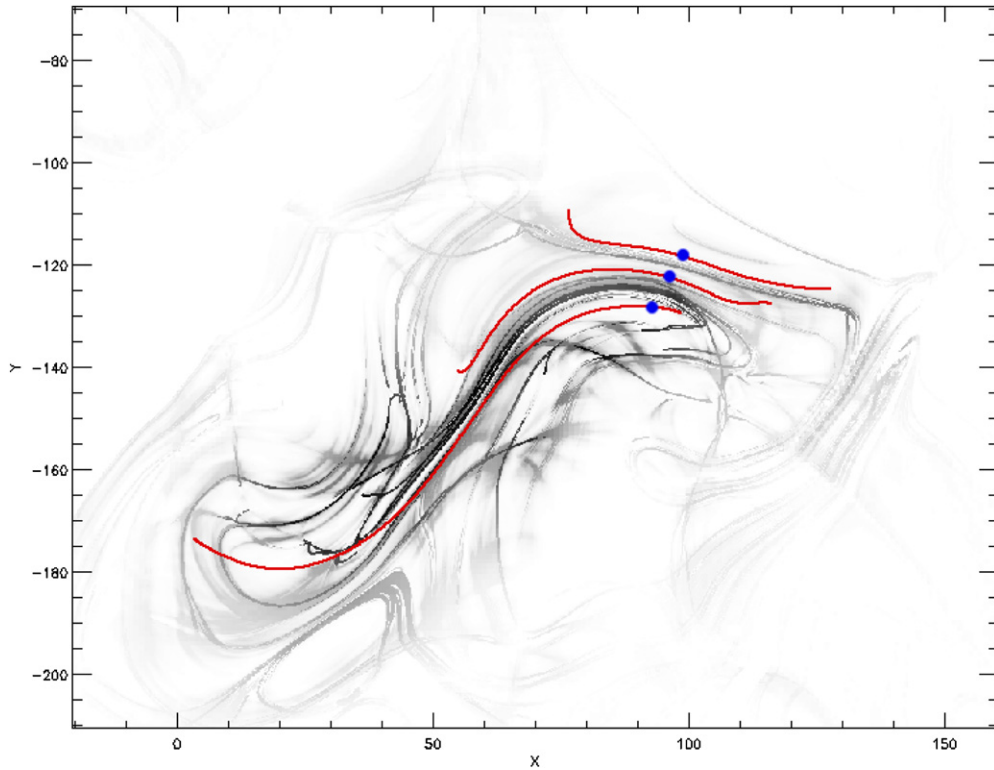


**Figure 9.**  $JQ$  map for February 10,  $z = 10$ . Three sample field lines have been traced from the blue dots on the figure on different sides of prominent QSLs. It is apparent that although the field lines are launched close together they diverge significantly with distance to where they connect to the photosphere. (A color version of this figure is available in the online journal.)

S-shaped QSLs associated with the flux rope. This model is characterized by the highest axial flux while the poloidal flux in the region at the time of this model is  $10^{10} \text{ Mx cm}^{-1}$  as for the majority of the rest of the models (see Table 1). At the same time, the flux distribution and the initial flux rope path produce a longer cavity which encompasses the previously more potential part of the region. On February 8, the flux rope is held down low by the potential arcade and at height  $z = 12$ , at which the horizontal slices are taken, the QSLs have started to shorten and straighten.

On February 9, the two regions have fully merged and some flux cancellation has taken place at the location where the two initial regions meet, as discussed in SvB09. This has removed one flux element that gave the characteristic curved shape to the QSLs on February 8. As a consequence, the PIL on February 9 is almost straight and the QSLs outlining the flux rope are also much straighter. Instead of having a hollow core distribution, as in the later models, the flux rope on February 9 is filled with current and this is also reflected in the  $JQ$  map; the area inside the flux rope is filled with many almost parallel QSLs. February 9 is the first day that we find comparatively extended areas along the flux rope where the field lines are concave-up and graze the photosphere; the so-called Bald Path Separatrix Surfaces (BPSS; Titov et al. 1993). The bald patch areas are aligned with the central QSLs in the flux rope. A much higher resolution calculation must be able to show that the  $Q$  value on these QSLs is highest and they may even be considered true separatrices. These BPSSs persist along the length of the sigmoid for the following three days and it is most likely that persistent reconnection at the BPSS heats the plasma on those field lines to coronal temperatures and gives the characteristic shape of the sigmoid as discussed in Titov & Démoulin (1999).

In addition, during this time the region is characterized by the presence of dark EUV and  $H\alpha$  filaments (SvB09). This is consistent with the observations and interpretations given in Aulanier et al. (1998) where BPSS explains the existence of  $H\alpha$  filaments. We can speculate that the continued reconnection at the BPSS and the flux cancellation in the region eventually elevate the flux rope away from a BPSS configuration, as we discuss in the next section.

As we approach the eruption on February 12, the main QSLs and the associated coronal X-ray emission has acquired a pronounced S-shape. In response to continued flux cancellation, the PIL has become curved again and the flux rope and associated QSLs are also curved. The flux ropes in these models are more elevated in response to the decreased strength of the potential arcade. Intense current concentration have started to develop on one edge of the flux rope. These current concentration exist for a couple of days before the eruption. However, because of the limited time resolution of the models and the accuracy of the fitting, we cannot say whether these strong QSLs develop into the ones that characterize the pre-eruption configuration, as discussed in the next section, since the models for the different days are independent of each other. We can say that the location where these QSLs are strongest is approximately the location of the flare cross section shown in the following figures.

As direct output of the modeling process we obtain the relative helicity (as defined in Bobra et al. 2008), total, potential, and free energy of the system. In Table 1, we list these values together with the errors determined on the basis of the parameters of neighboring models in the goodness-of-fit space. As in SvB09, our conclusion is still that, although the amount of free energy as a percentage of the total increases slightly toward the eruptions,

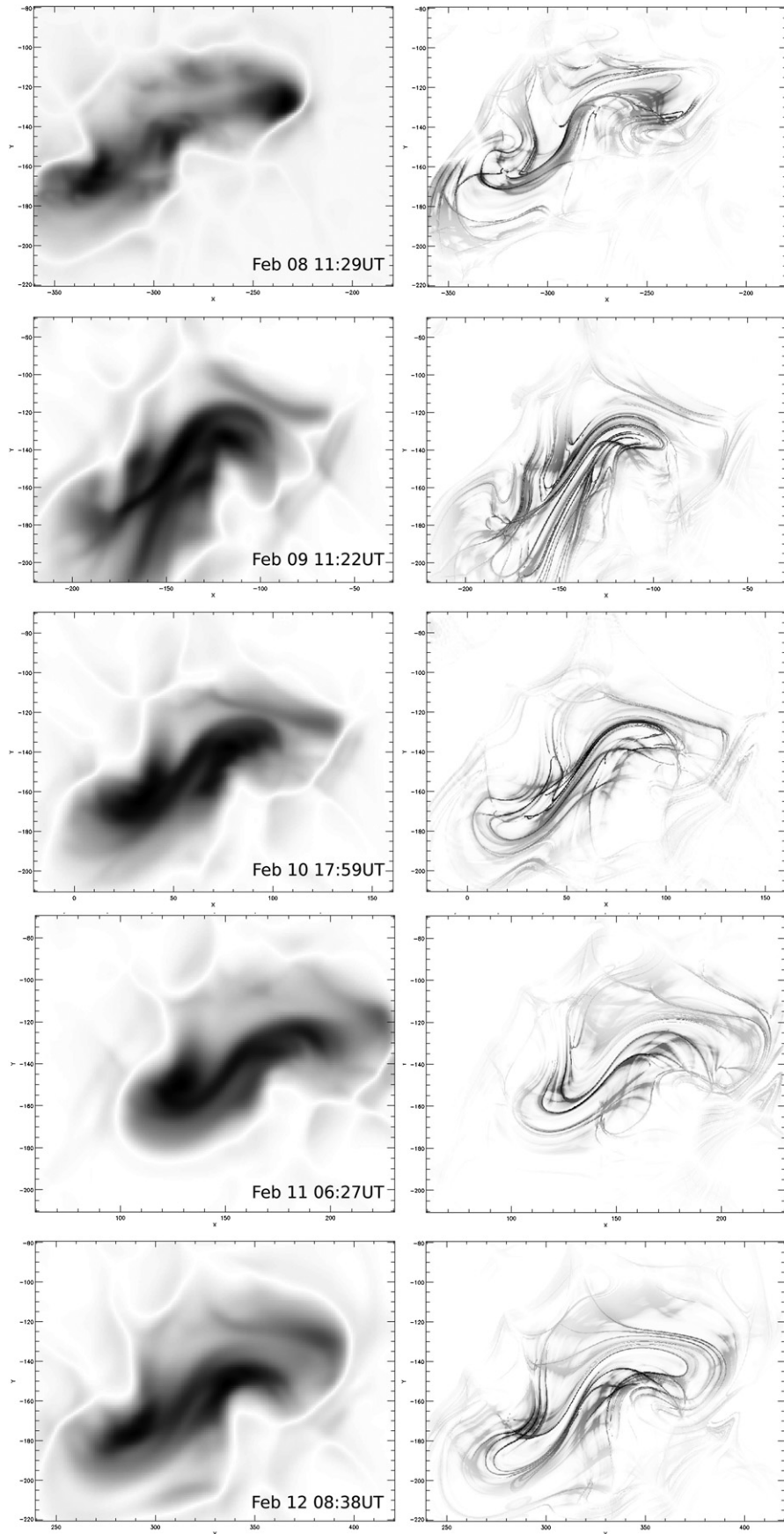


**Figure 10.** Sample current density (left column) and  $JQ$  (right column) maps for February 8, 9, 10, 11 (preceding the eruption), and February 12 08:39 UT (just after the eruption). All maps are at height  $z = 10$ .

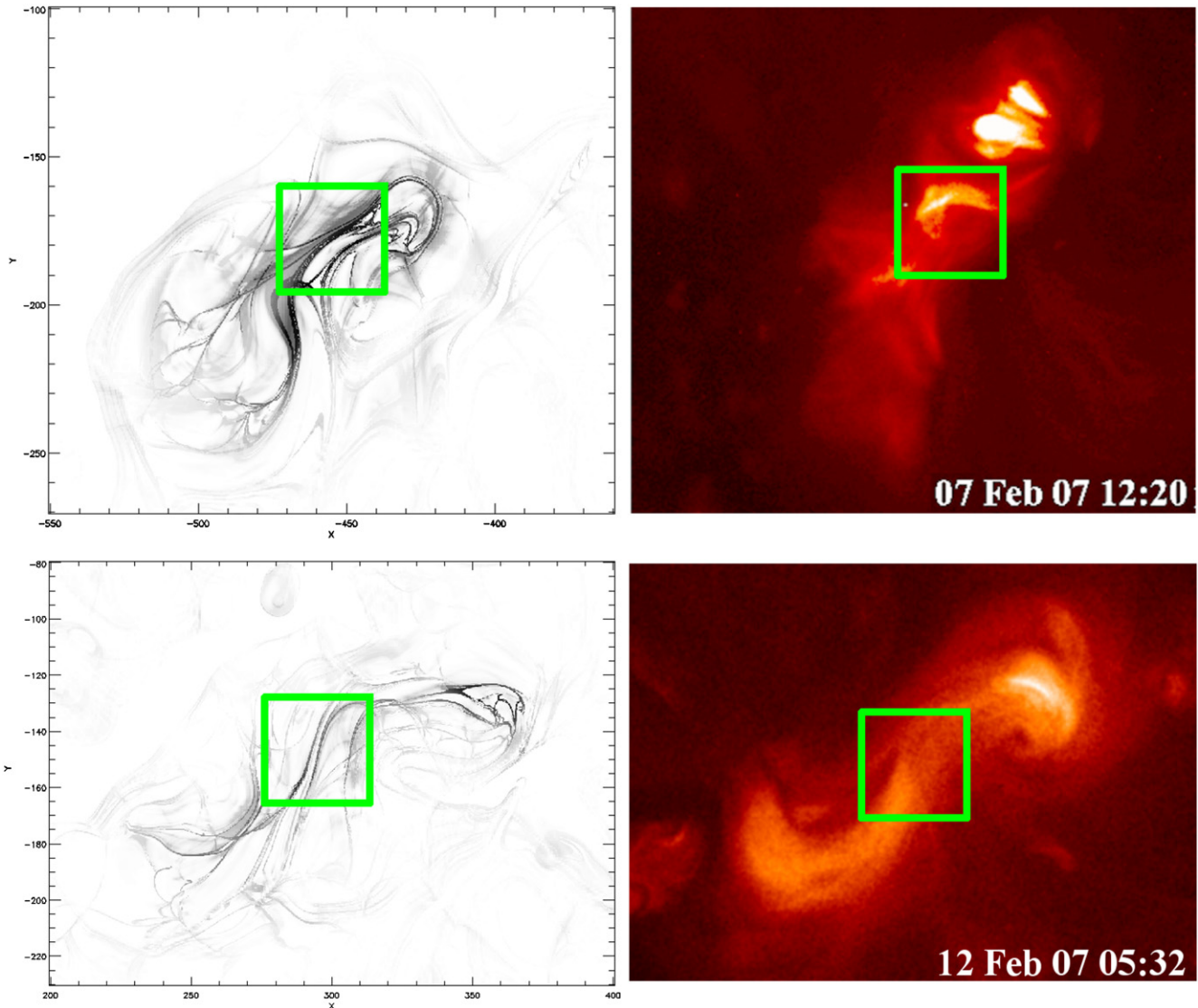


**Figure 11.**  $JQ$  plots for February 7 and 12 corresponding to the model just preceding the eruptions on those two days. Both maps are at  $z = 6$ . The corresponding XRT images are shown in the right column. The inferred locations of the two flares are inside the green box on all panels. (A color version of this figure is available in the online journal.)

this behavior is not consistent and cannot be used as a tracer of a possible eruption alone. The fact that our models are more sensitive to the axial flux in the flux rope than to the poloidal flux leads to uncertainty in the determined energies and helicities. For instance, the free energy on February 8, after the CME on February 7, is the highest, while the free energy is definitely higher on February 12, before the flare, as compared to the preceding days. Thus, one needs, in addition, to invoke information about the current distributions and the topology of the region in order to determine which configuration is likely to erupt.

## 7. MAGNETIC CONFIGURATION AT THE CME ONSET

On February 7 and 12 the region produced B-class flares followed by CMEs. In SvB09, we had knowledge only about the eruption on February 12. Our previous modeling revealed that the AR shows signs of pre-eruption behavior, such as slight build-up of helicity and free energy, before the event of February 12. Independently from the observations, our present modeling has shown that the model preceding the eruption on February 7

also shows indications of a pre-eruption configuration. Here, we identify the characteristics of the system that point to possible loss of equilibrium.

In Figure 11, we have shown the  $JQ$  plots together with the corresponding XRT images for February 7 and 12. The location of the flares in the images have been determined approximately based on the first loops that brighten in the beginning of the flares. Green squares encompassing the inferred location of the flares are shown on both the  $JQ$  maps and the images. The  $JQ$  plot for February 7 in the upper left panel of Figure 12 shows that the main QSLs associated with the flux rope are pinched at the northern part where they come together in a stronger QSL at a height of  $z = 6$ . Similarly, the main QSLs in the  $JQ$  plot for February 12 (lower panel) come together at a height of  $z = 4$ . We made cross sections through the flux rope, approximately perpendicular to its axis, and at several locations along the main QSL. The QSL cross section through the flux rope at the location of both flares shows a characteristic fully developed inverted teardrop shape (Figure 12). In 3D the QSL crosses itself at an X-line-like configuration (similar to Figure 5 from Titov 2007). This is characteristic of the so-called hyperbolic

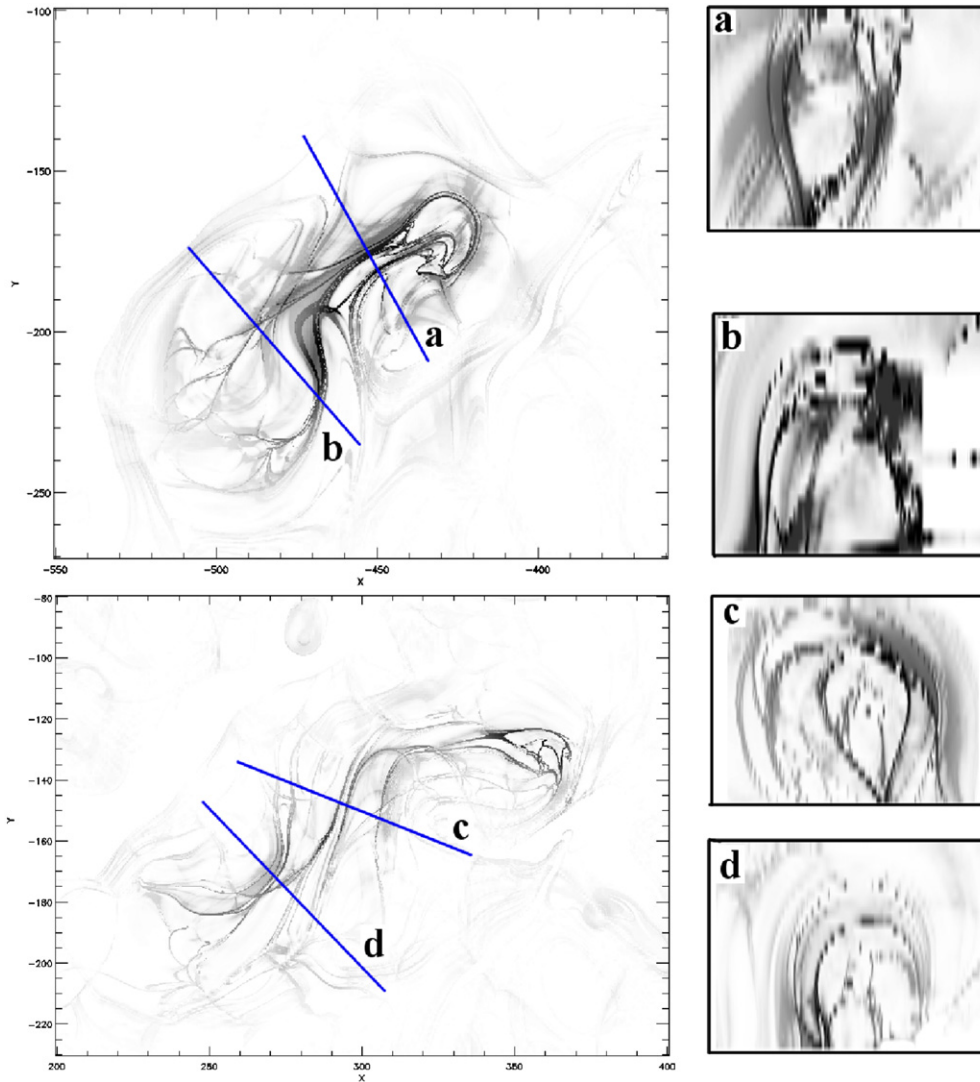


**Figure 12.** Same  $JQ$  plots as in Figure 11. Two vertical cross section for each model are taken at the location of the blue lines on the horizontal  $JQ$  maps. The first and third cross sections are at the location of the flares on February 7 and 12. The other two cross sections are taken away from the flare sites but before the flux rope starts to descent significantly toward the photosphere.

(A color version of this figure is available in the online journal.)

flux tube (HFT; Titov 2007) since the profile of the QSL layer, and consequently of the current layer that can potentially form there, has a hyperbolic four-way saddle shape (Figure 2, Titov 2007). In Titov’s work, in the absence of separatrices, the HFT represents the part of the magnetic volume where  $Q$  is highest. In this sense, it is the place where the sharpest current sheets can develop and reconnection is most likely to occur in an explosive manner. The current density distributions in the same cross sections (Figure 7) show similar shape, as discussed above, but they are much more diffuse than the QSLs. Here we suggest that the existence of an HFT is a topological tracer of a pre-flare configuration. Indeed, we show here that in our models both flares begin where the QSL cross sections show the typical HFT configuration. For February 12 we purposely studied the cross sections around the inferred location of the flare. However, for February 7 the presence of an HFT in the model prompted us to look back to the observations and discover the CME on February 7. In this sense, the presence of an HFT on February 7 forecasts the appearance of a flare and CME at the inferred location.

Figure 13 shows the connectivity of the field lines around the HFT. Generally there are four types of field lines that show up when one explores the four domains around the HFT as shown in Figure 1 of Démoulin et al. (1996b). The twisted long helical field lines that compose the body of the sigmoidal flux rope are located in domain (I) on the upper panel of Figure 13. These field lines appear S-shaped and run over the whole length of the sigmoid when projected on a horizontal view (lower panel). Field lines that are launched close to the photosphere on the left and right sides of the HFT (domains II and IV) appear J-shaped on the lower panel. Field lines that are rooted in the lower domain III, effectively below the HFT are short, low lying, and slightly inclined with respect to the PIL. This system of field lines is enveloped by a potential arcade which lies above the flux rope.

Tether cutting reconnection (Moore & Labonte 1980) between the J-like field lines is likely to occur at the HFT, which involves transfer of magnetic flux from domains II and IV into domains I and III. Observationally, this process forms short post-flare loops (similar to those in domain III) which run across the

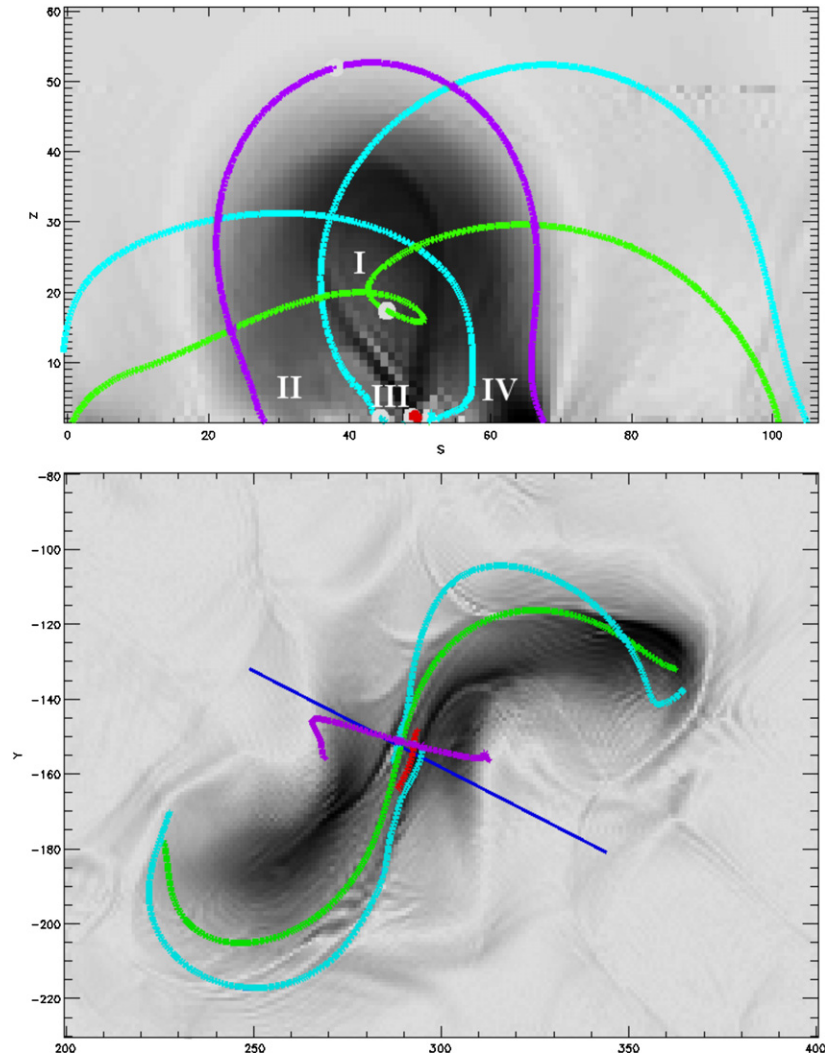


**Figure 13.** Current density plot at  $z = 12$  (upper panel) and cross section at the location of the dark blue line (lower panel). Characteristic field lines have been traced from the four domains in the cross section. The same field line in corresponding colors are shown on the horizontal plot. The purple field line belongs to the potential arcade. The two light blue field lines, launched from domains II and IV are J shaped. The green field line belongs to the inside of the flux rope (domain I) and has a characteristic S shape. A short red field line is located below the HFT in domain III.

(A color version of this figure is available in the online journal.)

PIL at an angle and connect the flare ribbons which outline the main QSLs on the photosphere. The HFT in the model for February 7 is formed only in small portion of the region where the main QSL cavity pinches. This is also the location where the two-J-like field lines come together and can be subject to tether cutting. For February 12 an HFT configuration exists over a larger portion of the flux rope, although the flare coincides with where the two oppositely directed J-like field lines come together at the most complete and elevated part of the HFT.

Both HFT configurations appear in models that precede the flare within eight hours in the case of the February 7 event and one hour for the February 12 event. The HFT is based on a best-fit model for the given day which happens to be also the last stable model, with a combination of flux rope magnetic fluxes that can just keep the system in balance with the potential arcade. This result points to the fact that at least in our static models, an HFT configuration forms well before the eruption and it persists until the balance is destroyed and the flare occurs.

The kink or torus instability are two options we have considered, via which the system can lose equilibrium. In SvB09, we have addressed the stability of this sigmoid with respect to the

ideal kink instability and we found that the twist in the flux rope is below the threshold for instability as determined by Török et al. (2004). Instead, suitable conditions for torus instability seem to exist in the region. In the case of February 12 we determine that the rate of decay of the potential arcade in height, as defined by Kliem & Török (2006), reaches a critical value of  $n = \partial \ln B / \partial \ln z = 1.5$  (Aulanier et al. 2010) at the edge of the flux rope. Hence, it is conceivable that continued reconnection at the HFT can allow the flux rope axis to rise into the torus instability domain. At this point the flux rope will not be restricted and will continue to rise which will sharpen the vertical current sheet at the HFT and cause more reconnection to take place. In this sense, the reconnection in the HFT and the ideal instability enter a positive feedback loop which eventually causes the CME in the region. In fact for February 12, we obtain a similarly good model which is already slightly unstable an hour before the eruption, which may indicate that the process of the rising of the HFT could have started some time before the eruption.

Away from the location of the flare the QSL cross sections do not show an HFT configuration (Figure 12). This is most obvious when looking at a cross section through the southern

part of the flux rope on February 7. Since we are dealing with real magnetic flux distributions, it is possible that the potential arcade is weaker at places where it allows the flux rope to expand more into the corona during the relaxation process, while at other places it is held low down. In looking along the flux rope axis we have stretches with BPSSs and HFT topology. For February 12 we have intermittent BPSS close to the location of the HFT. As mentioned above BPSSs are present in the sigmoid long before the HFT develops and although the region shows strong current concentrations, it remains stable over a few days before it erupts again on February 12. We do not have such observations for the time before the first eruption, since our first model is on February 6, just after the AR has rotated over the limb. Based on the above we infer that, in this case, the HFT is the topological feature that signifies a ready-to-erupt magnetic configuration, rather than a BPSS. We elaborate more on this conclusion in the last section.

### 8. A SCENARIO FOR CME ONSET

We suggest the following scenario for the onset of a CME in a decaying AR containing a flux rope. Initially, the magnetic configuration is in mechanical equilibrium: the magnetic pressure of the flux rope is balanced by the magnetic tension of the overlying coronal arcade. The configuration evolves slowly in response to the motions of magnetic elements in the photosphere and the cancellation of magnetic flux at PIL. Slow reconnection will occur at the BPSS between the flux rope and its surroundings. Such tether-cutting reconnection (Moore & Labonte 1980; Moore et al. 2001) will slowly transfer magnetic flux from the surrounding arcade to the flux rope, progressively elevating and strengthening the flux rope at the expense of the arcade. This slow evolution phase may last many days. During this phase the system is stable to ideal-MHD perturbations, and the magnetic field evolves quasi-statically through a series of force-free equilibrium states.

After some time the flux rope becomes so elevated that it no longer touches the photosphere and an HFT forms in the low corona below the flux rope. The HFT may form only along certain sections of the PIL. Tether-cutting reconnection will continue to occur at the HFT, causing the height of the HFT to slowly increase with time. During this phase the flux rope is still stable, but gradually approaches the marginally stable state where the system transitions from a stable to an unstable state. This slow evolution phase may last several hours and is consistent with the observed slow rise of filaments before they erupt (Sterling et al. 2007).

Eventually, the system reaches the marginally stable state and enters into the unstable regime, causing a loss of equilibrium of the magnetic configuration. The type of instability involved may depend on the degree of twist of the flux rope: kink instability for highly twisted ropes (e.g., Fan & Gibson 2004) or torus instability for less twisted ones (e.g., Kliem & Török 2006). In principle such instabilities can occur in ideal MHD, but on the real Sun magnetic reconnection is likely to play an important role in the dynamics. The fast evolution following loss of equilibrium is characterized by positive feedback between the tether-cutting reconnection at the HFT and the (ideal) instability of the system. The upward motion of the flux rope accelerates, causing a large increase in the rate of reconnection compared to the slow-rise phase.

According to the present model, the reconnection at flare onset involves J-shaped field lines that are transported to the reconnection site from the two sides. This is consistent with

the standard model for solar flares (see Figure 1 in Moore et al. 2001). The only difference is that we explicitly identify the reconnection site as an HFT. The above scenario is further supported by the 3D MHD simulations of Aulanier et al. (2010). The similarities between their MHD model and the models presented here will be further discussed in a future paper.

### 9. DISCUSSION AND CONCLUSIONS

Sigmoids have been shown to be the preferred sites for flares and CMEs (Canfield et al. 1999, 2007). Thus, it is prudent to study the evolution and eruption behavior of these regions. The sigmoidal shape is defined when the regions are observed in projection against the solar disk. In this case, due to the optically thin nature of the coronal plasma, we see the coronal loops that compose the sigmoid projected on top of each other. The only way to disentangle the magnetic field structure of such regions is to build NLFFF models which are most accurate in describing both the sheared and twisted core of the sigmoid and the overlying potential arcade. In this work, we determine the 3D coronal structure of a quiescent long-lasting sigmoid observed with XRT between 2007 February 6 and 12. The 3D field is provided by NLFFF models, based on the flux rope insertion method. One of the main advantages of the method is that field lines from a grid of models with different combinations of flux rope parameters can be fitted to observed coronal loops.

A direct output of the models is the magnetic free energy and helicity contained in the region. Traditionally, the buildup of free energy in ARs has been associated with regions in a pre-eruption phase. When the magnetic free energy reaches values similar to the typical energies released in flares, the region may become unstable and erupt. However, in SvB09 and in the above discussion we showed that the magnetic free energy cannot be used as an indicator of pre-eruption configuration alone. In the case of the studied sigmoid the region produces a flare and a CME when the free energy reaches about 20% of the total energy and then the free energy and the relative helicity continue to increase, not very consistently, toward the second eruption. Moreover, our models show that the region may become unstable when the magnetic free energy reaches above 15%, but the exact value at which the sigmoid loses equilibrium cannot be constrained. The buildup of free energy can also halt at about the same value for days or keep building up. Thus, we turn to topological analysis of the field in order to identify other features that can point to probable pre-eruption configuration and to identify the location of probable reconnection sites.

Null points and separatrix layers have been traditionally invoked as locations for buildup of sharp current sheets where the magnetic free energy can be released in an explosive manner in a massive reconnection process. However, Démoulin et al. (1997) have shown that just some of the erupting ARs have these specific topological features present before the eruption. The region we model in this work also does not possess any of the above special topologies although it produces two CMEs. So, we turn to analyzing QSL maps of the region. Since QSLs are ubiquitous parts of the volume where the field line linkage changes drastically, sharp current sheets can still accumulate in the presence of footpoint motions. We have shown that places with high values of the squashing factor,  $Q$ , in combination with other characteristics, can prove to be a good tracer of critical magnetic configurations.

Our present codes are not designed for fast QSL calculations and as a consequence our QSL maps reach only small values of the squashing factor ( $Q = 100$ ). 2D QSL maps were computed

at 25 different heights in the corona and stacked to obtain QSL cross sections through the flux rope for different days during the evolution of the region. We discussed some of the general properties of the QSL maps and the  $JQ$  plots, designed to bring out prominent QSLs at locations where the underlying extended current distribution peaks. We showed that the magnetic field and current vectors are aligned with prominent QSLs. Despite the fact that our models are static and cannot produce the very necessary sharp current sheets, the main QSLs coincide with peaks in the current density in our models. Both the main QSLs and the ridges in the current density outline a hollow core flux rope configuration. The shape of the QSLs is characteristic of flux rope configuration as discussed by Démoulin et al. (1996b).

We used the  $JQ$  plots to pick out prominent QSLs and to follow how the topology of the region evolves before the CMEs. We have shown that the main flux-rope-associated QSLs become more S-shaped in time which in combination with increased poloidal flux and helicity gives the characteristic S-shape and two-J field lines composing the sigmoid. Some strong current concentrations and high- $Q$  areas are seen in the region a couple of days before the eruption on February 12. BPSSs also exist at several location along the flux rope for a few days but they seem to be stable and not cause the eruptions.

We show that when the topology of the AR becomes dominated by a hyperbolic flux tube on February 7 and 12, the flux rope becomes unstable and erupts. The HFT is the location with highest  $Q$  and it is the most likely place where explosive reconnection can take place in this topology. In addition, the two oppositely directed J-like field lines come close together in the vicinity of the HFT and can possibly be subject to tether-cutting reconnection after the lift-off of the HFT. For both the February 7 and 12 CMEs the place in the model where we find a fully developed slightly elevated HFT is also the inferred location of the first flare loops that are seen by XRT and *STEREO*. Thus, we show that in this sigmoid, the HFT rather than the BPSS topology is characteristic of these eruptions.

Titov & Démoulin (1999) suggest that BPSSs are also likely places for the development of eruptive behavior since they represent true separatrices where reconnection can take place. Although several papers have relied on BPSS to explain the appearance of sigmoids (Magara 2006; Green et al. 2007, 2011; Fan & Gibson 2004), as we do for the days preceding the eruptions, we find only the simulation of Fan & Gibson (2004) to support eruptive behavior of a sigmoid facilitated by reconnection at BPSS-associated current sheet. However, the series of simulations by Fan & Gibson are all concerned with emerging flux ropes and best describe transient sigmoids which erupt by means of kink instability. On the other hand, Aulanier et al. (2010) and Su et al. (2011) have modeled decaying ARs with photospheric flux cancellation and they find the existence of characteristic inverted teardrop shapes in their current distributions in cross section just before the eruptions. Moreover, in the simulation of Aulanier et al. (2010) torus instability ensues which supports well our interpretation given above. In a purely observational study, Green et al. (2011) invoke the work of Gibson & Fan (2006) to infer that since the observed sigmoid is destroyed in the eruption it must have had an HFT topology. According to Gibson & Fan (2006) reforming sigmoids and filaments that remain after the eruption are associated with BPSS flux rope configurations where part of the sigmoid, and associated filament, remain behind close to the photosphere. In events where the sigmoid is destroyed in the process of the eruption the flux rope is carried away after

reconnection at the X-line under it. Observationally, as discussed in SvB09, this sigmoid gets destroyed and the filament in the H $\alpha$  images disappears after the eruption on February 12 (although the filament reappears a day later).

We propose a scenario where reconnection at the HFT is in positive feedback with a possible ideal torus instability, and this interplay allows the eruption to happen. Further, we show that the HFT first appears a few hours before the eruption. From the present analysis it is unclear what brings the system over the edge of stability. In this sense, we can use this type of modeling and topology analysis to point out that a flare might occur within a few hours to a day after this feature appears. A more statistical approach and the processing of more erupting sigmoidal regions may prove to be useful in consolidating the main conclusion from this work that the appearance of an HFT, in conjunction with suitable conditions for an instability, is the field configuration that leads to an imminent eruption. In addition, such a study with higher time resolution of the models can help in identifying the period over which an HFT can exist before the region becomes unstable. In the two eruptions seen in this region, the location of the HFT matches very well the location of the flare and hence we suggest that it can be used as a promising tracer of whether an eruption might occur in the near future and where. Moreover, if an HFT exists for large portion of the flux rope, we propose that the location where the HFT is most elevated might be the most probable location for reconnection.

*Hinode* is a Japanese mission developed, launched, and operated by ISAS/JAXA in partnership with NAOJ, NASA, and STFC (UK). Additional operational support is provided by ESA, NSC (Norway). This work was supported by NASA contract NNM07AB07C to SAO. We thank the referee for his useful comments which made the manuscript much better and E. Pariat for fruitful discussions. We thank L. Green for pointing us to the 2007 February 7 event.

## REFERENCES

- Amari, T., Luciani, J. F., Mikic, Z., & Linker, J. 2000, *ApJ*, **529**, 49
- Archontis, V., Hood, A. W., Savcheva, A., Golub, L., & DeLuca, E. 2009, *ApJ*, **691**, 1276
- Aulanier, G., Démoulin, P., Schmieder, B., Fang, C., & Tang, Y. H. 1998, *Sol. Phys.*, **183**, 369
- Aulanier, G., Pariat, E., & Démoulin, P. 2005, *ApJ*, **444**, 961
- Aulanier, G., Török, T., Démoulin, P., & DeLuca, E. E. 2010, *ApJ*, **708**, 314
- Baker, D., van Driel-Gesztelyi, L., Mandrini, C. H., Démoulin, P., & Murray, M. J. 2009, *ApJ*, **705**, 926
- Bhattacharjee, A., & Hameiri, E. 1986, *Phys. Rev. Lett.*, **67**, 206
- Bobra, M. G., van Ballegoijen, A. A., & DeLuca, E. E. 2008, *ApJ*, **672**, 1209
- Boozer, A. H. 1986, *J. Plasma Phys.*, **35**, 133
- Canfield, R. C., Hudson, H. S., & McKenzie, D. E. 1999, *Geophys. Res. Lett.*, **26**, 627
- Canfield, R. C., Kazachenko, M. D., Acton, L. W., et al. 2007, *ApJ*, **671**, 81
- Démoulin, P., Bagala, L. G., Mandrini, C. H., Hénoux, J. C., & Rovira, M. G. 1997, *A&A*, **325**, 305
- Démoulin, P., Hénoux, J. C., Priest, E., & Mandrini, C. H. 1996a, *A&A*, **308**, 643
- Démoulin, P., Priest, E., & Lomie, D. P. 1996b, *J. Geophys. Res.*, **101**, 7631
- Démoulin, P., van Driel-Gesztelyi, L., Schmieder, B., et al. 1993, *A&A*, **271**, 292
- Fan, Y., & Gibson, S. E. 2004, *ApJ*, **609**, 1123
- Fan, Y., & Gibson, S. E. 2006, *ApJ*, **641**, L149
- Fan, Y., & Gibson, S. E. 2007, *ApJ*, **668**, 1232
- Gibson, S. E., & Fan, Y. 2006, *ApJ*, **637**, L65
- Gibson, S. E., Fletcher, L., Del Zanna, G., et al. 2002, *ApJ*, **574**, 1021
- Golub, L., DeLuca, E., Austin, G., et al. 2007, *Sol. Phys.*, **243**, 63
- Green, L. M., Kliem, B., Török, T., van Driel-Gesztelyi, L., & Attrill, G. D. R. 2007, *Sol. Phys.*, **246**, 365

- Green, L. M., Kliem, B., & Wallace, A. J. 2011, *A&A*, **526**, A2
- Hesse, M., & Schindler, K. 1988, *J. Geophys. Res.*, **93**, 5559
- Janse, A. M., & Low, B. C. 2009, *ApJ*, **690**, 1089
- Janse, A. M., Low, B. C., & Parker, E. 2010, *Phys. Plasmas*, **17**, 092901
- Kliem, B., & Török, T. 2006, *Phys. Rev. Lett.*, **96**, 255002
- Leamon, R. J., Canfield, R. C., Blehm, Z., & Pevtsov, A. A. 2003, *ApJ*, **596**, L255
- Lau, Y. Y., & Finn, J. M. 1991, *ApJ*, **366**, 577
- Low, B. C., & Wolfson, R. 1988, *ApJ*, **324**, 574
- MacKay, D. H., & van Ballegoijen, A. A. 2006, *ApJ*, **641**, 577
- Magara, T. 2006, *ApJ*, **653**, 1499
- McKenzie, D. E., & Canfield, R. C. 2008, *A&A*, **481**, 65
- Mandrini, C. H., Démoulin, P., Bagala, L. G., et al. 1997, *Sol. Phys.*, **174**, 229
- Moore, R. L., & Labonte, B. J. 1980, in *IAU Symp. 91, Solar and Interplanetary Dynamics*, ed. M. Dryer & E. Tandberg-Hanssen (Dordrecht: Reidel), 207
- Moore, R. L., & Roumeliotis, G. 1992, in *Eruptive Solar Flares*, ed. Z. Svestka, B. V. Jakson, & M. E. Machado (Berlin: Springer), 69
- Moore, R. L., Sterling, A. C., Hudson, H. S., & Lemen, J. R. 2001, *ApJ*, **552**, 833
- Parker, E. N. 1972, *ApJ*, **174**, 499
- Parker, E. N. 1983, *ApJ*, **264**, 635
- Parker, E. N. 1987, *ApJ*, **318**, 876
- Parker, E. N. 1994, *Spontaneous Current Sheets in Magnetic Fields: With Applications to Stellar X-rays* (International Series in Astronomy and Astrophysics, Vol. 1; New York: Oxford)
- Pevtsov, A. A. 2002, *Sol. Phys.*, **207**, 111
- Priest, E., & Démoulin, P. 1995, *J. Geophys. Res.*, **100**, 443
- Priest, E., & Forbes, T. 1989, *Sol. Phys.*, **119**, 211
- Priest, E., & Forbes, T. 1992, *J. Geophys. Res.*, **97**, 1521
- Priest, E., & Forbes, T. 2002, *A&AR*, **10**, 313
- Rust, D. M., & Kumar, A. 1996, *ApJ*, **464**, L199
- Savcheva, A., & van Ballegoijen, A. 2009, *ApJ*, **703**, 1766
- Schindler, K., Hesse, M., & Birn, J. 1988, *J. Geophys. Res.*, **93**, 5547
- Schrijver, C. J., DeRosa, M. L., Metcalf, T., et al. 2008, *ApJ*, **675**, 1637
- Sterling, A. C., & Hudson, H. S. 1997, *ApJ*, **491**, L55
- Sterling, A. C., Moore, R. L., Berger, Thomas, E., et al. 2007, *PASJ*, **59**, 823
- Su, Y., Surges, V., van Ballegoijen, A. A., DeLuca, E. E., & Golub, L. 2011, *ApJ*, **734**, 53
- Su, Y., van Ballegoijen, A. A., Lites, B. W., et al. 2009, *ApJ*, **691**, 105
- Titov, V. S. 2007, *ApJ*, **660**, 863
- Titov, V. S., & Démoulin, P. 1999, *A&A*, **351**, 707
- Titov, V. S., Galsgaard, K., & Neukirch, T. 2003, *ApJ*, **582**, 1172
- Titov, V. S., Hornig, G., & Démoulin, P. 2002, *J. Geophys. Res.*, **107**, 1164
- Titov, V. S., Priest, E., & Démoulin, P. 1993, *A&A*, **276**, 564
- Török, T., Kliem, B., & Titov, V. S. 2004, *A&A*, **413**, L27
- van Ballegoijen, A. A. 1999, in *Magnetic Helicity in Space and Laboratory Plasmas*, ed. M. R. Brown, R. C. Canfield, & A. A. Pevtsov (Washington, DC: AGU), 213
- van Ballegoijen, A. A. 2004, *ApJ*, **612**, 519
- Wang, H., Yan, Y., Sakurai, T., & Zhang, M. 2000, *Sol. Phys.*, **197**, 263
- Yeates, A. R., MacKay, D. H., & van Ballegoijen, A. A. 2009, *Sol. Phys.*, **247**, 103